Journal of Materials Chemistry A

ROYAL SOCIETY OF CHEMISTRY

PAPER

Published on 30 June 2026

Cite this: *J. Mater. Chem. A*, 2026, **14**, 32895

Carbon dioxide reduction catalyzed by a photoactive bimetallic zirconium/cerium metal–organic framework built with a (thieno)thiophene linker

Giacomo Provinciali, *[ab] Maria Vincenza Pagliaro, [a] Beatrice Muzzi, [a] Lorenzo Poggini, [abc] Benny Danilo Belviso, [d] Anna Mauri, [e] Simona Galli, [eb] Lorenzo Donà, [f] Bartolomeo Civalleri, [f] Giuliano Giambastiani [cb] and Andrea Rossin *[ab]

The development of efficient and stable photocatalysts for CO_2 reduction remains a major challenge in solar fuel production. Herein, we report the synthesis and characterization of the novel bimetallic zirconium/cerium metal–organic framework $[Zr_{5.96}Ce_{0.04}O_4(OH)_8(H_2O)_4(TTp)_4]$ [H_2TTp = (thieno)thiophene-2,5-dicarboxylic acid, **Zr/Ce_TTp**] used for CO_2 reduction under UV-visible light irradiation. Crystal structure characterization confirms the formation of a mixed-metal framework of **fcu** topology with uniform element distribution. The material is porous (BET SSA = 1054 $m^2\ g^{-1}$) and shows a good thermodynamic affinity for CO_2 [Q_{st} = 23.0 kJ mol^{-1}]. Optical and electrochemical characterization studies reveal enhanced light-harvesting ability and superior charge separation properties compared to the monometallic analogues **Zr_TTp** and **Ce_TTp**. Under simulated solar irradiation, **Zr/Ce_TTp** displays significant photocatalytic activity for CO_2 reduction to CO (5.8 μmol $g^{-1}\ h^{-1}$) with no need of auxiliary co-catalysts, while no activity is observed for the individual metal-based materials. The improved performance is attributed to the synergistic interaction between the redox-active Ce centers and the robust Zr nodes, as well as the light-absorbing capability of the H_2TTp linker. Periodic DFT calculations support the experimental findings, highlighting the role of open Ce^{III} sites in CO_2 activation and the improved spatial separation of the frontier orbitals in the bimetallic framework that reduces $e–h^+$ recombination with respect to its homometallic analogues. These results highlight the potential of heterometallic MOFs featuring π-conjugated heterocyclic linkers as promising platforms for solar-driven CO_2 valorization.

Received 5th May 2026
Accepted 30th June 2026

DOI: 10.1039/d6ta03759c

rsc.li/materials-a

Introduction

The increasing concentration of atmospheric CO_2 resulting from fossil fuel combustion poses severe environmental challenges. As a greenhouse gas, CO_2 absorbs and re-emits infrared radiation, thereby reinforcing the greenhouse effect and contributing to a sustained increase in global average temperature. This warming is linked to serious environmental consequences, including sea-level rise, shifts in precipitation regimes and water cycles, degradation of ecosystems, ocean acidification and increased frequency and intensity of extreme weather events. The 30th United Nations Climate Change Conference (COP30) held in Belém (Brazil) in November 2025 (ref. 1) broke new ground by explicitly referencing fossil fuels in its final agreement. The final declaration also emphasized the need for urgent action to keep the 1.5 °C goal of global temperature increase by 2050 within reach. While waiting for alternative energy sources to be prevalent in driving the world economy, huge efforts are being made to reduce CO_2 concentration in the atmosphere far below the current 430 ppm value (recorded in April 2026). Among the emerging strategies to address this issue, Carbon Capture and Utilization (CCU) is an innovative approach to mitigate climate change by capturing CO_2 emissions from industrial sources or the atmosphere and converting them into valuable products.[2–4] CCU aims to

[a]*Istituto di Chimica dei Composti Organometallici (CNR-ICCOM), Via Madonna del Piano 10, Sesto Fiorentino (Firenze), 50019, Italy. E-mail: giacomo.provinciali@cnr.it; andrea.rossin@cnr.it*

[b]*Consorzio Interuniversitario per la Scienza e Tecnologia dei Materiali, INSTM, Via Giusti 9, 50121 Firenze, Italy*

[c]*Dipartimento di Chimica "Ugo Schiff", Università di Firenze, Via della Lastruccia 3-13, Sesto Fiorentino (Firenze), 50019, Italy*

[d]*Istituto di Cristallografia (CNR-IC), via Amendola 122/o, 70125 Bari, Italy*

[e]*Dipartimento di Scienza e Alta Tecnologia, Università degli Studi dell'Insubria, Via Valleggio 9, 22100 Como, Italy*

[f]*Dipartimento di Chimica, Università di Torino, via P. Giuria 7, 10125 Torino, Italy*

transform CO_2 into fuels, chemicals, building materials, or polymers, creating a circular carbon economy. This strategy not only reduces greenhouse gas emissions but also provides economic incentives by turning waste CO_2 into commercially useful resources, bridging environmental sustainability with industrial innovation. The photocatalytic conversion of CO_2 into value-added fuels or chemicals using solar energy represents a highly attractive and sustainable solution.[5] However, the chemical inertness of CO_2 and complex multielectron transfer processes required for its activation remain a major obstacle in achieving high efficiency and selectivity in relevant photocatalytic systems.[6] In recent years, Metal–Organic Frameworks (MOFs) have garnered significant attention as promising photocatalysts for CO_2 reduction, owing to their high surface area (and related CO_2 adsorption capacity that increases their local concentration in proximity of the catalytically active sites), tunable pore architecture and the modularity of their building blocks.[7–14] The relevance of MOFs in contemporary chemistry and materials science has been brought to worldwide attention after the assignment of the Nobel Prize in Chemistry 2025 to Susumu Kitagawa, Richard Robson and Omar Yaghi for their pioneering work in this area.[15] Both metal nodes and organic linkers in MOFs can be rationally designed to optimize light absorption, charge separation, and catalytic activity. In particular, zirconium-based MOFs such as UiO-type frameworks[16–19] have shown excellent structural stability, water tolerance and chemical robustness, while cerium-containing MOFs offer the additional benefit of redox-active centers due to the Ce^{III}/Ce^{IV} couple, which can enhance charge carrier dynamics.[20–23] Several studies have highlighted the potential of combining two metals to create heterometallic MOFs with improved photocatalytic properties,[24–26] but systematic investigations on such systems remain limited. Equally crucial to MOF photoactivity is the choice of the organic linker. While conventional aromatic dicarboxylates provide structural integrity, they typically exhibit poor visible light absorption. The incorporation of heteroaromatic units such as thiazole- or thiophene-based linkers has emerged as an effective strategy to enhance light-harvesting capabilities through π-conjugation extension and sulfur-mediated electronic effects.[27] Nevertheless, the synergistic combination of photoactive linkers and redox-active heterometallic nodes in a single MOF architecture is still underexplored, particularly for photocatalytic CO_2 reduction. Herein, we report the design and synthesis of the novel bimetallic MOF of minimal formula $[Zr_{5.96}Ce_{0.04}O_4(OH)_8(H_2O)_4(TTp)_4]$ (**Zr/Ce_TTp**) built with (thieno)thiophene-2,5-dicarboxylic acid (H_2TTp, Scheme 1) as the organic linker. This framework integrates the structural stability of $[Zr_6]$ clusters found in all zirconium-based MOFs, the redox versatility of the cerium centers and the light-harvesting capability of the H_2TTp linker.[28–30] Through a combination of structural, spectroscopic, and electrochemical characterization, we demonstrate that **Zr/Ce_TTp** exhibits enhanced optical absorption, efficient charge separation and significantly improved photocatalytic CO_2 reduction performance under simulated solar light compared to its monometallic analogues **Zr_TTp** and **Ce_TTp**. Overall, this study highlights the potential of heterometallic MOFs with heterocyclic π-conjugated linkers as next-generation photocatalysts for solar fuel production.

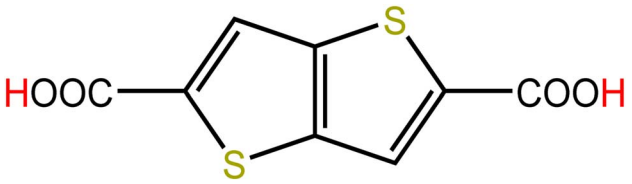

Scheme 1 Molecular structure of the linker used in this study: (thieno)thiophene-2,5-dicarboxylic acid (H_2TTp).

Experimental section

Materials and methods

Zirconium chloride/oxychloride ($ZrCl_4/ZrOCl_2$), cerium ammonium nitrate [$(NH_4)_2Ce(NO_3)_6$, CAN], trifluoroacetic acid (HTFA) and *N*,*N*-dimethylformamide (DMF) were purchased from Sigma-Aldrich and used as received. The glycinate-capped cluster $[Ce_6O_4(OH)_4(HGly)_8(NO_3)_4(H_2O)_6Cl_8]\cdot 8H_2O$ (HGly = NH_3CH_2COO)[31] and the heterocyclic ligand thieno[3,2-*b*] thiophene-2,5-dicarboxylic acid (H_2TTp)[32] were prepared following literature procedures. FT-IR spectra (KBr pellets) were recorded on a PerkinElmer Spectrum BX Series FTIR spectrometer, in the 4000–400 cm^{-1} range, with a 2 cm^{-1} resolution. UV-vis absorption diffuse reflectance spectra of H_2TTp, **Zr_TTp**, **Ce_TTp** and **Zr/Ce_TTp** in the solid state were recorded from 250 to 600 nm with a Jasco V-770 spectrophotometer equipped with a 60 mm integrating sphere and a PbS detector (ISN-923), using an interval wavelength of 1 nm. Photoluminescence spectra of the linker and MOFs in the solid state were recorded with a JascoFP-8300 spectrofluorometer equipped with a 150 W xenon arc lamp. The samples were irradiated at the wavelength corresponding to their maximum absorbance, as revealed by the absorption spectrum. The optical band gaps of **Zr_TTp**, **Ce_TTp** and **Zr/Ce_TTp** in the solid state were determined from the onset of their absorption spectra. The values are 3.4, 3.0 and 3.4 eV, respectively. Elemental analyses were performed using a Thermo FlashEA 1112 Series CHNS-O elemental analyzer with an accepted tolerance of ±2% on carbon (C), hydrogen (H), nitrogen (N) and sulfur (S). ICP analyses were performed with an ICP OES Agilent 5800 instrument, by dissolving 50 mg of sample in 3 mL of a HCl aqueous solution 37% m/m and 6 mL of a HNO_3 aqueous solution 65% m/m, followed by dilution to a total volume of 50 mL. Zirconium and cerium were quantified considering their absorption at 343.823 and 418.659 nm, respectively. Thermogravimetric analyses (TG-DTG) were performed under a N_2 flow (100 mL min^{-1}) at a heating rate of 5 K min^{-1} with an EXSTAR Thermogravimetric Analyzer Seiko 6200. The latter was coupled with a ThermoStarTM GSD 301T mass spectrometer for mass analysis of the volatile species. Scanning Electron Microscopy (SEM) images were acquired using a Tescan GAIA 3 FIB/SEM equipped with an EDS-X-ray microanalysis system (EDAX, AMETEK, USA) and with the TEAM EDS Basic Software Suite TEAM™. For the sample

preparation, a spatula tip of the powder was dropped on a stub covered by adhesive SEM tape. Excess (unadhered) sample was then removed by applying a gentle flux of Ar on the surface of the stub. The as-prepared sample was analyzed without further conductive coating, using an e-beam energy of 10 keV. Scanning Transmission Electron Microscopy (STEM) High-Angle Annular Dark Field (HAADF) images were acquired using a Thermo Fisher Scientific Talos F200X G2 microscope equipped with a high-brightness X-FEG field emission gun (80–200 keV), operated at an accelerating voltage of 200 kV. Images were collected with a Panther annular STEM detector using a convergent beam with a semi-angle of 10.5 mrad and a camera length of 330 mm. Energy-Dispersive X-ray Spectroscopy (EDS) maps were obtained with a Super-X spectrometer equipped with four 30 mm^2 silicon drift detectors, providing a total collection angle of 0.7 srad. All electron microscopy characterization studies were performed at the CeME electron microscopy facility (CNR-ICCOM, Florence). The nature and purity of all the batches employed for the functional characterization were assessed through powder X-ray diffraction (PXRD). PXRD preliminary measurements were carried out in the 2–50° 2θ region with a Panalytical X'PERT PRO diffractometer equipped with a Ni filter in the diffracted beam, a PIXcel© solid state detector and a sealed X-ray tube (Cu Kα, $\lambda = 1.5418$ Å). Slits were used in both the incident (Soller slits aperture: 0.25°; divergence slit aperture: 0.5°) and the diffracted (anti-scatter slit aperture: 7.5 mm) beam. The generator was operated at 40 kV and 40 mA. X-Ray fluorescence (XRF) spectra of a powdered sample (*ca.* 5 mg) of **Zr_TTp** were acquired in air using a PANalytical Minipal2 instrument equipped with a sealed X-ray tube having a Cr-anode. The generator was set to 30 kV and 3 μA. The XPS characterisation was carried out in a UHV chamber ($10^{-9}/10^{-10}$ mbar) equipped with non-monochromatized Al radiation ($h\nu =$ 1486.6 eV, VSW-TA1) combined with a hemispherical electron/ion energy analyser (VSW-HA100 with a 16-channel detector). The operating power of the X-ray source was 144 W (12 kV and 12 mA), and photoelectrons were collected normal to the sample surface, maintaining the angle between the analyser axis and the X-ray source fixed at 54.5°. All samples were adsorbed on carbon tape, and the XPS spectra were acquired in the fixed analyser transmission mode with a pass energy of 44.0 eV. The *CasaXPS* software was used to analyse the spectra, and a linear or Shirley function was used for the background correction.[33] The deconvolution of XPS spectra has been performed by applying a combination of Gaussian and Lorentzian functions (70/30 ratio) for S 2p and Zr 3d and a Lorentzian asymmetric lineshape for Ce 3d. All the binding energies (BE in eV) were calibrated upon fixing C 1s of the carbon tape at 285.1 eV.[34] X-ray Absorption Spectroscopy (XAS) measurements were performed on **Zr_TTp** and **Zr/Ce_TTp** powdered samples.[35] Data collection was performed at room temperature in transmission mode at the BM31 beamline of the European Synchrotron Radiation Facility (ESRF) by using Si(111) monochromator crystals, a beam size of 10 mm × 0.6 mm, and Ar-filled ionization chambers to measure the incident and transmitted X-ray intensity. Energy calibration was performed using metallic Zr foil. For each sample, two consecutive energy scans were collected and merged, centered on the Zr K-edge, from 17.85 KeV to 19.0 KeV, so as to cover both the XANES and EXAFS ranges. The resulting averaged spectra were normalized and background-subtracted by using Athena and Artemis, respectively, included in the Demeter XAS suite (ver. 0.9.26).[36] EXAFS fitting was based on theoretical scattering paths generated by the Free Energy Force Field (FEFF) from two structural models: a regular octahedral [Zr_6] cluster (derived from the crystal structure of **Zr_TTp**, disregarding the presence of missing linkers) and an axially distorted octahedral [Zr_6] cluster (obtained from DFT calculations, *vide infra*). While the former model consists of six Zr atoms with identical chemical environments, the latter features two Zr atoms in a different chemical environment compared to the four Zr atoms in the equatorial plane. The structure including the axially distorted model also contains [Zr_5Ce] inorganic units, in which one of the Zr atoms along the direction of distortion is replaced by a Ce atom; the latter was used to account for the contribution of Ce-containing scattering paths in the fit. The first-shell coordination of the Zr atoms is very similar in each of the models included in both the PXRD-retrieved and DFT-optimized structure and consists of eight O atoms surrounding each Zr atom at distances ranging from 2.1 to 2.3 Å. Only single scattering paths showing a contribution over 10% of the total EXAFS signal of the model (rank parameter calculated by using the FEFF) were considered for the fitting. Data below 1.2 Å in the direct space were removed from each dataset and *k*-weights of 3 and 2 were used for background removal of **Zr_TTp** and **Zr/Ce_TTp**, respectively. EXAFS data were fitted in the reciprocal space at a *k*-weight equal to 2 and over the range of 2.5–14.5 $Å^{-1}$ (**Zr_TTp**) and 2.6–12.0 $Å^{-1}$ (**Zr/Ce_TTp**). The range of the direct space considered for the fitting was 1.2–4.0 Å for both samples. The same amplitude reduction factor ($S_0{}^2$) and edge shift (ΔE_0) were used for all paths, whereas interatomic distances and Debye–Waller factors were refined. Coordination numbers were set according to the structural model. Co-refining of the background spline was also performed at the end of the fitting procedure.

Synthesis of Zr_TTp

$ZrCl_4$ (FW = 233.02 g mol^{-1}, 0.104 g, 0.44 mmol), 0.5 mL of trifluoroacetic acid and H_2TTp (FW = 228.0 g mol^{-1}, 0.102 mg, 0.44 mmol, 1 equiv.) were dissolved in 12 mL of DMF. After 15 minutes of stirring under ambient conditions, the solution was transferred into a 19 mL Teflon-lined stainless-steel container and heated to $T = 403$ K for 72 hours. After cooling, the off-white powder of **Zr_TTp·DMF** was collected, washed with ethanol (EtOH, 3 × 10 mL) and petroleum ether (3 × 10 mL) and finally dried under a nitrogen stream at room temperature. Yield: 0.112 g {82%, based on the minimal formula [$Zr_6O_4(OH)_8(H_2O)_4$(TTp)$_4$] 2(DMF)}. Elemental analysis calcd. (%) for [$Zr_6O_4(OH)_8(H_2O)_4$(TTp)$_4$] 2(DMF), $C_{38}H_{38}N_2O_{34}S_8Zr_6$ (MW = 1870.53 g mol^{-1}): C, 24.4; H, 2.0; N, 1.5; S, 13.7; Zr, 29.3. Elemental analysis found (%): C, 24.1; H, 1.6; N, 1.3; S, 14.0; Zr, 29.0 (ICP). IR bands (KBr pellet, cm^{-1}, Fig. S1): 1640(s), 1577(vs), 1482(vs),

1395(vs), 1325(vs), 1176(m), 1099(w), 1059(w), 897(w), 861(w), 762(m), 688(m), 648(m), 466(m).

Synthesis of Ce_TTp

Following the synthetic protocol described by the group of Stock for the preparation of other Ce^{IV} MOFs starting from pre-formed [Ce_6] clusters,[37] H_2TTp [FW = 228.0 g mol^{-1}; 0.061 g, 0.26 mmol, 6 equiv.] was dissolved in DMF (14 mL) and the resulting yellow solution was brought to T = 373 K under magnetic stirring. The glycinate-capped cluster $[Ce_6O_4(OH)_4(HGly)_8(NO_3)_4(H_2O)_6Cl_8]\cdot 8H_2O$ [FW = 2349.1 g mol^{-1}; 0.104 g, 0.044 mmol] was suspended in distilled water (1.5 mL), and the suspension was slowly added to the linker hot DMF solution. Immediate formation of a yellow solid precipitate of **Ce_TTp·DMF** was observed. Stirring at T = 373 K was maintained for an additional 15 min to complete the reaction. After that time, the reaction mixture was cooled to room temperature and the solid was recovered after centrifugation (4000 rpm, 5 min), washed with EtOH (3 × 10 mL) and petroleum ether (3 × 10 mL) and finally dried under a nitrogen stream at room temperature. Yield: 0.102 g {85%, based on the minimal formula $Ce_6O_4(OH)_4(Gly)_2(TTp)_5$ 6 (DMF)}. Elemental analysis calcd. (%) for $Ce_6O_4(OH)_4(Gly)_2(TTp)_5$ 6 (DMF), $C_{62}H_{64}O_{38}N_8S_{10}Ce_6$ (FW = 2690.51 g mol^{-1}): C, 27.7; H, 2.4; N, 4.2; S, 11.9, Ce, 31.2. Elemental analysis found (%): C, 27.4; H, 2.3; N, 4.2; S, 11.8; Ce, 31.5 (ICP). IR bands (KBr pellet, cm^{-1}, Fig. S1): 1654(vs), 1563(vs), 1484(vs), 1383(vs), 1325(vs), 1225(m), 1174(m), 1101(m), 1061(m), 893(w), 865(w), 766(s), 684(m), 565(s), 522(m), 430(m).

Synthesis of Zr/Ce_TTp

$ZrCl_4$ (FW = 233.02 g mol^{-1}, 0.051 g, 0.22 mmol) and CAN (FW = 548.22 g mol^{-1}, 0.120 g, 0.22 mmol) were dissolved in 8 mL of DMF. Then, 0.25 mL of trifluoroacetic acid and H_2TTp [FW = 228 g mol^{-1}; 0.050 g, 0.22 mmol, 1 equiv. with respect to each metal] were added to the solution. After 15 minutes of stirring under ambient conditions, the solution was transferred into a 19 mL Teflon-lined stainless-steel reactor and heated to T = 403 K for 72 hours. After cooling, the light yellow powder of **Zr/Ce_TTp·DMF** was collected, washed with EtOH (3 × 10 mL) and petroleum ether (3 × 10 mL) and finally dried under a nitrogen stream at room temperature. Yield: 0.085 g {82%, based on the minimal formula $Zr_{5.96}Ce_{0.04}O_4(OH)_8(H_2O)_4(TTp)_4$ 2(DMF)}. Elemental analysis calcd. (%) for $Zr_{5.96}Ce_{0.04}O_4(OH)_8(H_2O)_4(TTp)_4$ 2(DMF), $C_{38}H_{38}O_{34}N_2S_8Zr_{5.96}Ce_{0.04}$ (FW = 1872.5 g mol^{-1}): C, 24.4; H, 2.0; N, 1.5; S, 13.7; Zr, 29.0; Ce, 0.3. Elemental analysis found (%): C, 25.0; H, 1.4; N, 1.4; S, 12.0; Zr, 28.1 (ICP); Ce, 0.2 (ICP). IR bands (KBr pellet, cm^{-1}, Fig. S1): 1624(m), 1569(s), 1488(vs), 1399(s), 1204(w), 1176(m), 1111(w), 1005(w), 897(w), 861(w), 783(m), 764(s), 694(m), 656(s), 470(m).

Powder X-ray diffraction structure characterization of Zr_TTp and Zr/Ce_TTp

Powdered samples of the two MOFs (*ca.* 20 mg) were deposited in the cavity of a silicon zero-background sample holder 0.2 mm deep. The PXRD pattern for the structural characterization of **Zr_TTp** was acquired under ambient conditions in the 2θ range of 5.0–105.0° with steps of 0.02° and a time per step of 10 s using a Bruker AXS D8 Advance vertical-scan $\theta:\theta$ diffractometer equipped with a sealed X-ray tube (Cu K_α, λ = 1.5418 Å), a Bruker Lynxeye linear position-sensitive detector, Soller slits (aperture = 2.5°) in the primary and secondary beam, a fixed divergence slit (aperture = 0.5°), an anti-scatter slit (aperture = 8 mm) and a filter of nickel in the diffracted beam. The generator was set to 40 kV and 40 mA. The PXRD pattern for the structural characterization of **Zr/Ce_TTp** was acquired under ambient conditions in the 2θ range of 1.5–105.0° with the diffractometer quoted in the Materials and Methods section but equipped with a divergence slit of aperture 0.125°. All the data treatments described in the following section were carried out using the software *TOPAS-R v.3*.[38] The purity and crystallinity of the samples were assessed by performing a whole powder pattern refinement with the Le Bail method[39] employing, as a starting point, the space group ($Fm\bar{3}m$) and unit cell parameter of UiO-66.[40] The instrumental contribution to the peak profile was described with the fundamental parameters approach (FPA).[41] The sample contribution to the peak profile was modelled convoluting Lorentzian and Gaussian functions. The background was described with a Chebyshev polynomial function. During the first steps of the structure characterization, the atoms of the node were assigned the fractional coordinates of the corresponding atom in UiO-66. For simplicity, the OH^- ligands were described as oxygen atoms. In **Zr/Ce_TTp**, given the very low amount of cerium retrieved by elemental analysis (Zr : Ce = 5.96 : 0.04), the Zr : Ce molar ratio was fixed to that value, the presence of Ce^{III} (36%, as from XPS) was disregarded, and the cerium and zirconium atoms occupying the same octahedral vertex were assigned the same fractional coordinates. In both MOFs, the independent portion of TTp^{2-} ($\frac{1}{4}$ of the linker) was modelled as a rigid body with idealised bond distances and angles.[42] Its centre of mass was located in [0.25 0 0.25] (Wyckoff letter *d*). The vicariant C–H group and sulphur atom were superimposed, halving their site occupation factor (s.o.f.). The orientation of the linker, initially assigned based on the crystal structure of UiO-66, was refined (consequently adjusting the s.o.f. of the atoms reproduced by symmetry). A refined, isotropic thermal displacement factor, $B(M)$, was assigned to the metal atoms, while that of the other atoms was calculated to be $B(M)$ + 2 Å^2. The instrumental contribution to the peak profile was modelled with the FPA. The sample contribution to the peak profile was described convoluting a Lorentzian function to spherical harmonics. The smeared electron density in the pores was modelled with a DMF molecule, built as a rigid body with idealised bond distances and angles[43] whose position and orientation were found with the simulated annealing approach,[44] and whose s.o.f. was refined. The presence of missing-linker defects was verified at this stage for both MOFs refining the s.o.f. of the linker atoms, except that of the oxygen atom, which is present as a OH^-/H_2O ligand when TTp^{2-} is missing to guarantee electroneutrality (the presence of chloride anions derived from the zirconium salt used in the synthesis was excluded based on XRF, Fig. S2). During the structure refinement, carried out with the Rietveld method,[45]

the unit cell axis and the coefficients of the Chebyshev function and of the functions describing the sample contribution to the peak profile were refined, together with the non-special fractional coordinates of the atoms of the cluster and of the centre of mass of the DMF molecule. Its orientation and that of the linker were refined too. The graphical result of the final stage of the Rietveld refinements is shown in Fig. S3. As for **Ce_TTp**, the very limited degree of crystallinity discouraged any attempt of PXRD characterization of its average crystal structure.

Crystallographic information for **Zr_TTp**, $Zr_6O_4(OH)_{7.8}(H_2O)_{3.8}(TTp)_{4.1}\cdot 3DMF$, $C_{41.8}H_{44.6}N_3O_{35}S_{8.2}Zr_6$, FW = 1959.28 g mol^{-1}, cubic, $Fm\bar{3}m$, a = 23.1754(4) Å, V = 12447.5(7) Å^3, $Z = 4$, $Z' = 0.021$, $\rho = 1.0$ g cm^{-3}, $F(000) = 3870.4$, $R_{Bragg} = 0.4\%$, $R_p = 1.3\%$, $R_{wp} = 1.7\%$, for 4965 data and 54 parameters in the 5.7°–105.0° 2θ range. CCDC no. 2536450.

Crystallographic information for **Zr/Ce_TTp**, $Zr_{5.96}Ce_{0.04}O_4(OH)_{7.4}(H_2O)_{3.4}(TTp)_{4.3}\cdot 3.3DMF$, $C_{44.3}H_{45.9}N_{3.3}O_{35.3}S_{8.6}Zr_{5.96}Ce_{0.04}$, FW = 2014.39 g mol^{-1}, cubic, $Fm\bar{3}m$, $a = 23.1379(4)$ Å, $V = 12387.2(7)$ Å^3, $Z = 4$, $Z' = 0.021$, ρ = 1.1 g cm^{-3}, $F(000) = 3982.1$, $R_{Bragg} = 1.2\%$, $R_p = 3.1\%$, R_{wp} = 4.0%, for 4975 data and 49 parameters in the 5.5°–105.0° 2θ range. CCDC no. 2536451.

N_2 and CO_2 adsorption isotherms

A powdered sample (*ca.* 40 mg) of **Zr/Ce_TTp** was activated at T = 423 K under high vacuum (10^{-6} torr) for 24 h before the measurement. The Brunauer–Emmett–Teller (BET) specific surface area, pore size distribution and pore volume (V_{tot} and V_{micro}) were estimated by volumetric adsorption with an ASAP 2020 Micromeritics instrument, using N_2 as the adsorbate at T = 77 K. For the BET specific surface area calculation, the 0.01–0.1 p/p_0 pressure range of the isotherm was used to fit the data. Within this range, all the Rouquerol consistency criteria[46] are satisfied. The material (micro)porosity was determined from the N_2 adsorption isotherm using a NLDFT method (Tarazona approximation) and assuming a cylindrical pore shape (typical of metal oxides). CO_2 adsorption isotherms were recorded at T = 273 K, 298 K and 323 K at a maximum pressure of 1.2 bar. The CO_2 isosteric heat of adsorption (Q_{st}) of **Zr/Ce_TTp** was calculated from the three isotherms according to the differential form of the Clausius–Clapeyron equation:[47,48]

$$\left[\frac{\partial(\ln p)}{\partial\left(\frac{1}{T}\right)}\right]_\theta = -\frac{Q_{st}}{R} \quad (1)$$

where R is the gas constant (8.314 J K^{-1} mol^{-1}).

Photoelectrochemical measurements

Photocurrent (PC), Mott–Schottky (M–S) plots, linear scan voltage (LSV) and electrochemical impedance spectroscopy (EIS) were measured with a Princeton 2273A potentiostat/galvanostat, using a standard 3 electrode system composed of a $Ag/AgCl_{sat}(KCl_{sat})$ as the reference electrode (RE), a platinum-wire counter electrode (CE) and a catalyst-coated FTO glass as the working electrode (WE) (with an area of about 2 cm^2). All tests were conducted in a 0.5 M Na_2SO_4 aqueous solution as the electrolyte. The WE was prepared by dropcasting 1 mL of photocatalyst ink solution (1 mg_{cat} $mL_{iso\text{-}propanol}^{-1}$) on the FTO support. A 300 watt Xe lamp (mKs-Newport) was used as the light source with an intensity of 100 mW cm^{-2} to perform PC measurements. PC analyses were performed by registering the current at an applied potential of 0.6 V *vs.* $Ag/AgCl_{sat}(KCl_{sat})$. M–S plots were recorded without light at an arc amplitude of 10 mV and frequency of 1 kHz, while EIS measurements were carried out from 1000 kHz to 0.01 Hz at a potential of −1.1 V *vs.* $Ag/AgCl_{sat}(KCl_{sat})$. LSVs were registered at 10 mV s^{-1} between −0.6 and −1.2 V.

CO_2 photoreduction tests

The photocatalytic carbon dioxide reduction experiments were performed in a cylindrical quartz reactor (volume 18 mL) at ambient temperature (T = 298 K). 5 mg of catalyst was ultrasonically dispersed in 5 mL of degassed MilliQ water. 99. 999% pure CO_2 was injected into the reaction system for 30 min to remove air and saturate the solution with CO_2 only. Finally, the reactor was closed with a rubber cap equipped with a silicone septum. A 300-W Xe lamp (mKs-Newport) was used as the light source with an intensity of 100 mW cm^{-2}. Stirring was started when the sample was irradiated with light (UV-vis region). The evolved gas was sampled after five hours and analyzed using an off-line gas chromatograph (Shimadzu GC-2010) equipped with a thermal conductivity detector (TCD) and a molecular sieve (5 Å) column. Finally, **Zr/Ce_TTp** was used for a photocatalytic recycling test where the evolved gas was sampled every 5 h irradiation time. After the end of each run, fresh CO_2 was bubbled in the reactor for 15 min, the quartz Schlenk was closed and the system was irradiated again. Additional control experiments were conducted under identical conditions, including dark tests, blank runs without a catalyst, irradiation of the free H_2TTp linker, experiments under an inert He atmosphere and tests with a 1 : 1 physical mixture of **Zr_TTp** and **Ce_TTp** using the same total catalyst loading.

Computational details

Periodic DFT calculations were performed at the PBEsol0-3c level of theory,[49] as implemented in the CRYSTAL code.[50] PBEsol0-3c is a cost-effective composite method that has been successfully applied to predict several properties of MOFs.[51] It is based on the PBEsol[52] exchange–correlation functional hybridized with 25% of Fock exchange and combined with a double-zeta quality basis set for solid-state systems. It is also augmented with the D3 (ref. 53) and gCP[54] corrections to account for van der Waals interactions and to remove the basis set superposition error (BSSE), respectively. For the numerical integration of the exchange–correlation term, 75 radial points and 974 angular points (XLGRID) in a Lebedev scheme were adopted. The SCF convergence was set to 10^{-7} and 10^{-10} hartree during geometry optimization and vibrational frequency calculations, respectively. The Pack–Monkhorst/Gilat shrinking factors for the diagonalization of the Kohn–Sham matrix in reciprocal space were set to 2. The truncation criteria

(TOLINTEG) for the bielectronic integrals (Coulomb and exchange series) were set to 7 7 7 7 25. On the optimized structures, vibrational frequencies were calculated at the Γ point from a mass-weighed Hessian matrix obtained by numerical differentiation of the analytical first derivatives. From the vibrational frequencies, the zero-point vibration energy (E_{ZPV}) and the thermal contribution to the enthalpy, H_T, at $T = 298$ K and standard pressure p were calculated. The *JMol*[55] software was used for plotting the frontier orbitals (HOCO and LUCO) and the electrostatic potential (ESP) maps.

Results and discussion

Synthesis and preliminary characterization of Zr_TTp, Zr/Ce_TTp and Ce_TTp

With the aim of preparing MOF materials with a photoactive linker that may act as antenna for UV-visible light absorption and harvesting, we chose the bicyclic fused (thieno)thiophene aromatic core. (Thieno)thiophene-2,5-dicarboxylic acid has previously been used by other groups for the construction of rare-Earth-[56–59] or 3d-metal-based[60–62]-MOFs and coordination polymers. The zirconium MOF **Zr_TTp** of cubic **fcu** topology typical of the UiO-6x family[40] was prepared as an off-white microcrystalline powder through a conventional solvothermal synthesis carried out in *N*,*N*-dimethylformamide (DMF) and starting from either zirconium chloride ($ZrCl_4$) or zirconium oxychloride ($ZrOCl_2$) as the metal source in the presence of trifluoroacetic acid (HTFA) as the crystal modulator. The cerium(IV) analogue **Ce_TTp** was instead prepared using a milder approach. The reaction between H_2TTp and a pre-formed [Ce_6] glycinate cluster was carried out in a round-bottom flask at ambient pressure, leading to immediate precipitation of the deep yellow product upon mixing the reagents in hot DMF ($T =$ 373 K). This synthetic methodology was developed by the group of Stock and co-workers in 2018 (ref. 37) and it proved to be very efficient and versatile for the preparation of many Ce^{IV} MOFs that would be otherwise inaccessible using traditional starting materials like cerium ammonium nitrate (CAN). Indeed, in our attempts at a direct solvothermal synthesis using CAN as the starting salt under the same experimental conditions used for **Zr_TTp** the reaction provided a completely different white crystalline phase (presumably, a Ce^{III} coordination polymer with an unknown crystal structure). Finally, the mixed-metal sample **Zr/Ce_TTp** was prepared by co-dissolving $ZrCl_4$ and CAN together with H_2TTp under the same solvothermal conditions used for **Zr_TTp**. This strategy allows the simultaneous incorporation of both metal ions into a single phase. To assess the robustness and reproducibility of the synthetic method, the preparation of **Zr/Ce_TTp** was independently repeated three times, yielding consistent results in terms of yield and morphology. In particular, the amount of cerium present in different **Zr/Ce_TTp** batches is very low but consistent with a relative Zr/Ce atomic ratio equal to 197 ± 17 as estimated through EDX data (Fig. S4–S6). Different relative $ZrCl_4$/CAN stoichiometric ratios were also explored; however, only the equimolar Zr/Ce precursor ratio afforded a photo-catalytically active MOF. In the IR spectra (Fig. S1), the typical ν(COO) stretching bands of carboxylate groups at 1640, 1654 and 1624 cm^{-1} for **Zr_TTp**, **Ce_TTp** and **Zr/Ce_TTp**, respectively, are indicative of the linker presence in the solid. A small red shift with respect to the free linker (1667 cm^{-1} for H_2TTp) is observed, typically occurring after carboxylate coordination to a metal center. As inferred from a comparison of the relevant PXRD data (Fig. S7), the three MOFs are isostructural and show the typical UiO-66 pattern with intense, and well-defined reflections below $2\theta = 10°$ and a well-resolved pattern up to 45°. Small differences in the peak maxima are found, reasonably due to the different ionic radii of Zr^{IV} (72 pm) and Ce^{IV} (103 pm) that mirrors the slightly larger unit cell dimensions for **Ce_TTp** in comparison with those of **Zr_TTp** and **Zr/Ce_TTp**. Given the very low cerium content in the latter (*vide infra*), the peak positions of **Zr/Ce_TTp** are practically indistinguishable from those of **Zr_TTp**. In contrast, **Ce_TTp** exhibits significantly broader and less intense diffraction peaks, unveiling the limited crystallinity of this material. Indeed, the presence of diffuse scattering, particularly in the low-angle region, might indicate short-range ordering or the formation of nanocrystalline domains. This behavior is commonly observed in cerium-based MOFs, where Ce^{III}/Ce^{IV} redox dynamics, larger ionic radii and different coordination preferences often result in crystal structures with a limited long-range order;[63] though to a lower extent, diffuse scattering also characterizes the PXRD patterns of the other two MOFs. Notably, no PXRD peaks attributable to cerium oxide or Ce-MOF phases were detected in the **Zr/Ce_TTp** pattern, indicating the formation of a single-phase bimetallic MOF without phase segregation. This was also confirmed by Scanning Transmission Electron Microscopy (STEM) imaging of solid samples, combined with Energy-Dispersive X-ray Spectroscopy (EDS) elemental analysis (Fig. S8). As shown in Fig. 1, scanning electron microscopy (SEM) and STEM-high angle annular dark field (HAADF) images revealed that the material consists of slightly aggregated polyhedral micro and nanocrystals with sizes ranging from 100 to 400 nm and exhibiting smooth surfaces and uniform shape. The crystal size retrieved on processing the images perfectly matches with that inferred from the application of the Debye–Scherrer equation on the main peak at $2\theta = 6.66°$ of the PXRD pattern (≈110 nm). Elemental mapping recorded for a single nanocrystal confirms the presence of all the expected elements Zr, Ce, and S, uniformly distributed throughout the entire particle volume. In particular, the overlapping EDS maps of Zr and Ce indicate a homogeneous incorporation of both metal centers within the MOF framework, with no evidence of phase segregation or core–shell architectures. The even distribution of S and C further confirms the successful integration of the TTp^{2-} linker into the MIXMOF. For completeness, elemental distribution maps were further collected for more than five nanocrystals, confirming the overall homogeneity of the sample. These results provide strong evidence for the formation of a true mixed-metal framework rather than a physical mixture of Zr- and Ce-based phases and support the structural integrity of the **Zr/Ce_TTp** material at the nanoscale.

Thermogravimetric analysis (TGA) combined with mass spectrometry (MS) of the exhaust reveals that **Zr/Ce_TTp** is

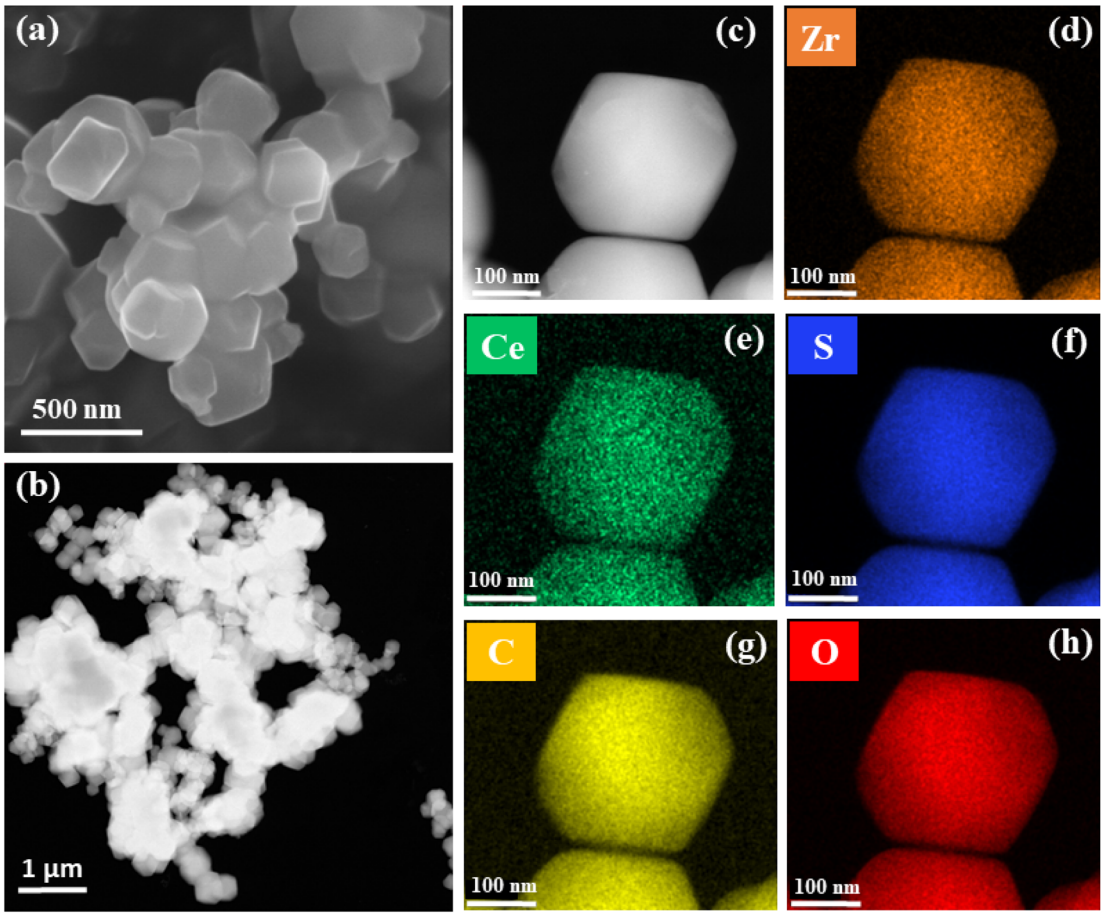

Fig. 1 (a) SEM and (b and c) TEM (HAADF) images of **Zr/Ce_TTp**; (d–h) STEM-EDX element (Zr, Ce, S, C, and O) mapping distribution for the chemical composition analysis of **Zr/Ce_TTp**.

thermally stable until $T_{dec} \approx 733$ K, with this temperature falling in the typical range of other zirconium MOFs.[40] After an initial weight loss ($T < 383$ K) due to physisorbed humidity and residual washing solvents (ethanol and petroleum ether), another loss of ~8.0 wt% (Fig. S9a) is recorded in the 413–623 K range, ascribed to clathrated DMF coming from the synthesis (theoretical weight loss = 7.8 wt%). This is further confirmed by the presence of the typical DMF peak at $m/z = 73$ a.m.u. observed in the mass spectra of the volatiles in the same temperature range (Fig. S9b). Intriguingly, DMF loss takes place at two different temperatures (first loss at $T = 490$ K; second loss at $T = 724$ K, close to T_{dec}). This reveals that part of the DMF molecules may be coordinated to the Ce^{III} centers present in the sample, to fill the coordination vacancy that forms after cerium partial reduction (*vide infra*). Elemental CHN-S and ICP analyses provide a lower C and S content with respect to the theoretical value expected for the ideal $[M_6O_4(OH)_4(L)_6]$ formula unit. The best compromise can be found if we consider a defective MOF with missing linker defects where the $[M_6]$ nodes are 8-coordinated: $[M_6O_4(OH)_8(H_2O)_4(L)_4]$. The defective coordination sites are thus saturated by –OH/H_2O couples. This formula is also in line with the TGA-MS results and with the metal content coming from ICP analysis. The values found for **Zr/Ce_TTp·DMF** lead to the final formula $[Zr_{5.96}Ce_{0.04}O_4(OH)_8(H_2O)_4(TTp)_4]$ 2(DMF) (theoretical wt% Zr = 29.0; experimental = 28.1; theoretical wt% Ce = 0.3; experimental = 0.2). In order to assess the oxidation state of zirconium, cerium and sulphur in the MOFs, a high-resolution X-ray Photoelectron Spectroscopy (XPS) characterisation was carried out on samples of the three materials. **Ce_TTp** contains both Ce^{IV} and Ce^{III} in a 69% : 31% ratio (Fig. S10 and Table S1), in line with the relevant literature;[64,65] the sulphur atoms of the (thieno)thiophene ring were found to be in the sulphide form (S^{2-}), with a single component centred at a Binding Energy (BE) of 164 eV as expected;[66–68] the semi-quantitative analysis also revealed values in line with what was expected (Table S1). In contrast, **Zr_TTp** is mostly composed of Zr^{IV}[69,70] as predicted for this kind of material with a single component, plus its spin–orbit coupling at BE = 183.0 eV; sulphur is in the sulphide form as expected for a thiophene moiety (at BE = 164.2 eV) as found in **Ce_TTp**. The semi-quantitative analysis is reported in Table S1. Finally, XPS characterisation of **Zr/Ce_TTp** (Fig. 2) reveals a hybrid behaviour intermediate between the **Ce_TTp** and **Zr_TTp** homometallic reference systems. As expected, zirconium is present as Zr^{IV} (BE = 183.0 eV), while cerium exhibits a mixed-valence state, with Ce^{IV}/Ce^{III} contributions of approximately 64% and 36%

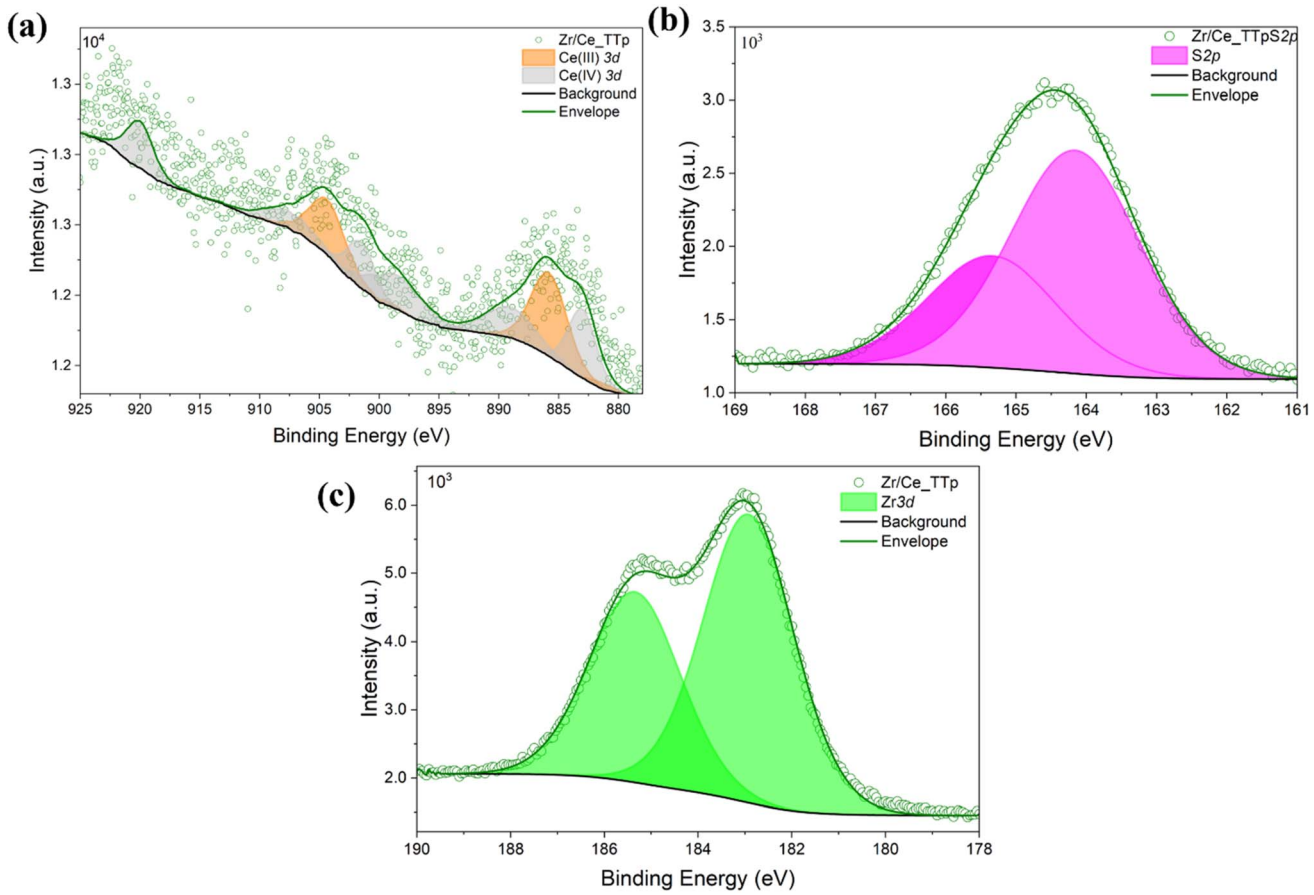

Fig. 2 High resolution Ce 3d (a), S 2p (b) and Zr 3d (c) XPS spectra of **Zr/Ce_TTp**.

respectively, as reported in Table S1. The sulphur atom was found to be in the same sulphide oxidation state as those of **Ce_TTp** and **Zr_TTp** with a component centred at BE = 164.1 eV. The semiquantitative analysis of **Zr/Ce_TTp** shows good agreement with the theoretical one, as reported in Table S1.

Crystal structure characterization from combined PXRD diffraction and EXAFS analysis

A successful in-house PXRD structural characterization confirmed that both **Zr_TTp** and **Zr/Ce_TTp** are isostructural with UiO-66. As suggested in the previous section based on a visual comparison of their diffraction patterns (Fig. S7), the two materials show comparable unit cell axis values [23.1754(4) and 23.1379(4) Å for **Zr_TTp** and **Zr/Ce_TTp**, respectively], in agreement with the very low cerium content in the latter. In addition, due to the longer length of the TTp^{2-} linker with respect to the terephthalate linker of pristine UiO-66, the unit cell axis of the latter is *ca.* 10% shorter [20.700(<1) Å, determined at room temperature].[40] As in UiO-66, in **Zr_TTp** and **Zr/Ce_TTp** the nodes are composed of six Zr^{IV} or Zr/Ce^{IV} ions (Fig. 3a) arranged at the vertices of an octahedron of 3.5 Å edge. Each M^{IV} ion is coordinated by eight oxygen atoms, four belonging to the μ^3-O^{2-}/OH^- ligands [Zr–O distance = 2.150(4) Å in both MOFs] and four belonging to the carboxylate groups of TTp^{2-} [Zr–O distance = 2.223(9) Å and 2.216(2) Å in **Zr_TTp** and **Zr/Ce_TTp**, respectively]. In a non-defective UiO6x-type material, the [Zr_6] nodes are connected to twelve other clusters by

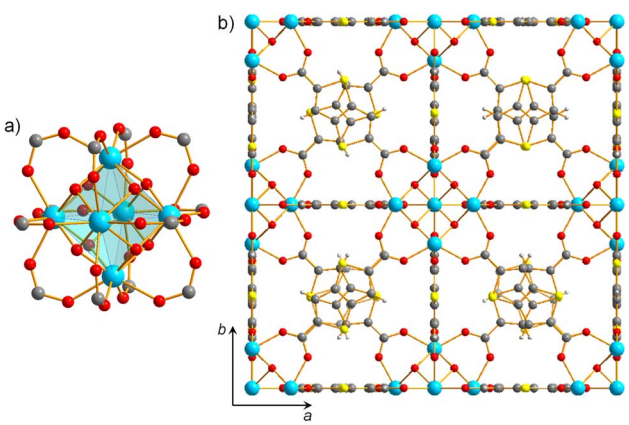

Fig. 3 Graphical representation of the crystal structure of **Zr/Ce_TTp**: (a) the node; (b) portion of the packing visualized along one of the crystallographic axes. For clarity, (i) an ideal crystal structure was employed, disregarding the missing linker defects and removing the S/C–H vicariance; (ii) the clathrated DMF molecules hosted in the pores were omitted. Element colour code: C, grey; H, light grey; O, red; S, yellow; Zr/Ce, light blue. The crystal structure of **Zr_TTp** is not distinguishable to the eye from that of **Zr/Ce_TTp**.

tetradentate TTp^{2-} spacers. This occurrence results in a 3D open framework (Fig. 3b) featuring tetrahedral and octahedral cavities which, in the present case, show diameters of *ca.* 5.3 and 10.5 Å, respectively.[71] In the real materials, the presence of missing linker defects was confirmed by the figures of merit lowering upon refining the linker site occupation factor: a percentage of missing linkers amounting to 32% and 28% was retrieved for **Zr_TTp** and **Zr/Ce_TTp**, respectively, corresponding to the presence of 4.1 and 4.3 TTp^{2-} linkers per cluster, respectively, in fair agreement with the result of the elemental analysis. The missing linkers were counterbalanced with OH^-/H_2O ligands, as the XRF qualitative analysis (Fig. S2) ruled out the presence of chlorine in the form of Cl^- anions deriving from the Zr^{IV} precursors used in the synthesis and potentially coordinated to the metal nodes. In **Zr/Ce_TTp**, the space-group imposed symmetry implies uniformly distributed metal ions, in agreement with the actual Zr/Ce distribution disclosed by STEM-EDX. DMF solvent molecules are hosted in the tetrahedral cavities. Disregarding them, the empty volume amounts to *ca.* 55% of the unit cell volume for both materials.[72]

The XAS and EXAFS spectra of **Zr_TTp** and **Zr/Ce_TTp** are shown in Fig. S11. EXAFS data (Fig. S11b) show a negligible contribution from the noise even at high wavenumber, indicating good quality for both samples. In both MOFs, the Fourier-transformed data (Fig. S11c) show a main peak at ~2.1 Å, consistent with the expected Zr–O distance in the first-coordination shell of the Zr atoms in the two materials, and a second peak at ~3.6 Å, indicative of a well-defined second coordination shell populated by heavier atoms, representing the intra-node Zr–Zr distances expected for the materials under investigation.

For both MOFs, based on the average crystal structure retrieved by PXRD, the absorber atoms (Zr) are expected to be located at the vertices of an octahedron, with each absorber coordinated by eight O atoms in the first coordination shell. While the relative arrangement of Zr atoms is known, it remains unclear whether the actual octahedron is regular or axially distorted, and whether the presence of Ce affects it. Therefore, both regular and axially distorted octahedral [Zr_6] nodes were used for the EXAFS fitting, and their agreement with the experimental data was evaluated using the *R*-factor statistics. Regardless of the MOF, the distorted polyhedron consistently yields a better *R*-factor than the regular one (with a reduction of 1.1% for **Zr_TTp** and 2% for **Zr/Ce_TTp**), suggesting that the

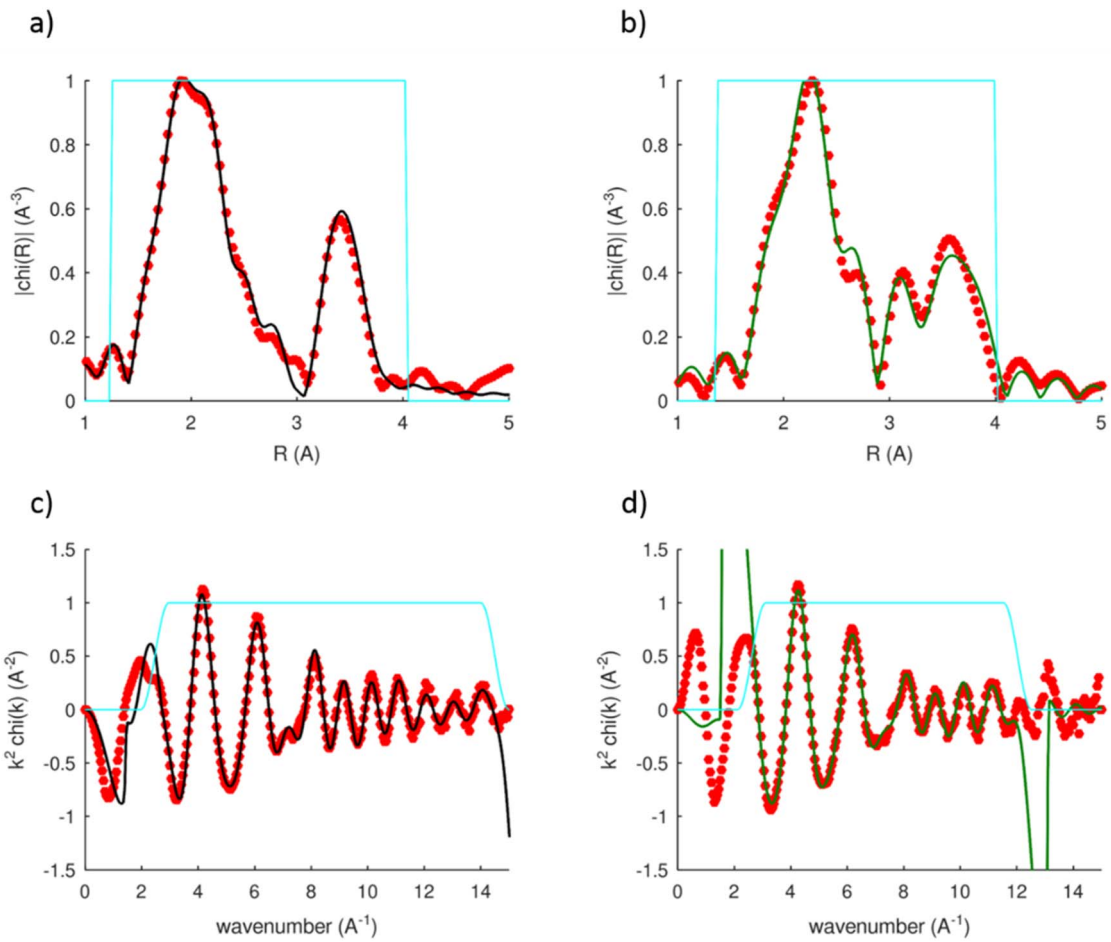

Fig. 4 EXAFS fitting results shown in the direct space (a and b) and reciprocal space (c and d) for **Zr_TTp** (a and c) and **Zr/Ce_TTp** (b and d). The observed data are represented by red dots, and the result of the fit is shown in black and dark green for **Zr_TTp** and **Zr/Ce_TTp**, respectively. Fitting windows are shown in cyan. Data are shown by using a *k*-weight of 2.

distorted octahedron provides a better description of the experimental data. This occurrence is in line with the defective MOF nature derived from the CHN-S and ICP elemental analyses and the PXRD structural characterization. Additional fits were attempted to include the contribution of Ce in the fitting for **Zr/Ce_TTp**. Considering for simplicity only one Ce/Zr replacement in the node and that the minimal formula obtained from elemental/ICP analysis is $[Zr_{5.96}Ce_{0.04}O_4(OH)_8(H_2O)_4(TTp)_4]$, 96% of the EXAFS signal is expected to arise from $[Zr_6]$ octahedra and the remaining 4% from $[Zr_5Ce]$ octahedra. However, the very low molar fraction of $[Zr_5Ce]$, including the contribution from the Zr–Ce path in the fit did not produce any appreciable change in the results. The results of the fitting procedure obtained by using the axially distorted octahedral $[Zr_6]$ cluster model are shown in Fig. 4 while the fit statistics, along with global and structural parameters resulting from the fitting are shown in Table S2.

The fitting procedure performed on the Zr atoms along the octahedron distorted axis [see "Structural parameters (axial Zr atoms)" in Table S2] gave a first coordination shell consisting of eight O atoms at 2.1 Å ($R_{O\_dist2.1}$ and $R_{O\_dist2.3}$) in the case of **Zr_TTp** and four O atoms at 2.3 Å ($R_{O\_dist2.1}$) plus four at 2.8 Å ($R_{O\_dist2.3}$) in the case of **Zr/Ce_TTp**. Although current XAS data cannot be exploited to confirm direct Ce/Zr replacement in **Zr/Ce_TTp**, the difference observed in the first shell suggests that the presence of a Ce atom moves the oxygen atoms away from Zr in **Zr/Ce_TTp** compared to **Zr_TTp**. An opposite trend is observed for the C atoms in the second coordination shell, whose distance relative to the axial Zr atoms ($R_{C\_dist3.3}$) decreases from 3.2 Å in **Zr_TTp** to 2.7 Å in **Zr/Ce_TTp**. Similarly, the C–Zr distance relative to the equatorial Zr atoms ($R_{Zr\_dist3.6}$) decreases from 3.5 to 3.3 Å in the presence of Ce. Focusing on the Zr atoms on the equatorial plane [see "Structural parameters (equatorial Zr atoms)" in Table S2], the fitting procedure provides very similar first shell coordination spheres for **Zr_TTp** and **Zr/Ce_TTp**, consisting of four O atoms at 1.8 Å ($R_{O\_dist2.1}$) and four O atoms at 2.2–2.3 Å ($R_{O\_dist2.3}$). The C atoms in the second shell are moved farther away in **Zr/Ce_TTp**, increasing the Zr–C distance ($R_{C\_dist3.3}$) from 3.0 Å in **Zr_TTp** to 3.7 Å in **Zr/Ce_TTp**. The distance between two equatorial Zr atoms ($R_{Zr\_eq\_dist3.6}$) is quite similar for the two materials (~3.5 Å). The high thermal factors observed for each path in both MOFs, despite the low amplitude reduction factor used in the fitting, may be due to the measurements being performed at room temperature. In summary, although the distorted octahedral model provides a better description of XAS data, the distances found between two equatorial Zr atoms and that between equatorial and axial Zr atoms is very close in **Zr_TTp** (3.56 against 3.54 Å) and slightly different in **Zr/Ce_TTp** (3.53 against 3.31 Å). Interestingly, for both MOFs the distance between equatorial and axial Zr atoms is lower than that between two equatorial Zr atoms, suggesting that the geometry distortion causes a compression of the octahedron. This effect is more pronounced in **Zr/Ce_TTp**. Moreover, these results suggest that the presence of Ce atoms increases the disorder of the first coordination shell for the axial Zr atoms and leads to a reduction of all Zr–Zr distances.

Textural property assessment through N_2 adsorption. Collection of CO_2 adsorption isotherms at variable temperatures

The porosity of **Zr/Ce_TTp** was analysed through N_2 volumetric adsorption at $T = 77$ K on a pre-activated powdered sample (Fig. 5a). The isotherm shape is of Type I, typical of microporous materials. The BET specific surface area after sample washing followed by thermal activation equals 1054 $m^2\ g^{-1}$; it is comparable to that of UiO-66 (BET SSA = 1187 $m^2\ g^{-1}$)[40] and $[Zn_2(TTp)_2(bpy)]$ published by Fedin and co-workers in 2022 (bpy = 4,4′-bipyridine; BET SSA = 952 $m^2\ g^{-1}$)[60] but much lower than that of $[Zn_4O(TTp)_3]$ (IRMOF-20; BET SSA = 3409 $m^2\ g^{-1}$)[62] or the mixed-linker MOF $[Zn_4O(TTp)(BTB)_{4/3}]$ (BTB^{3-} = 1,3,5-benzene(tribenzoic) acid, UMCM-2; BET SSA = 5200 $m^2\ g^{-1}$).[61] The total pore volume at $p/p^0 = 0.98$ equals 0.45 $cm^3\ g^{-1}$. The micropore size distribution evaluated through NLDFT methods has disclosed the presence of two main micropore sizes at w = 15 and 19 Å, slightly larger than those found in UiO-67 (ref. 73) but with the same dual nature (Fig. S12). The activated material

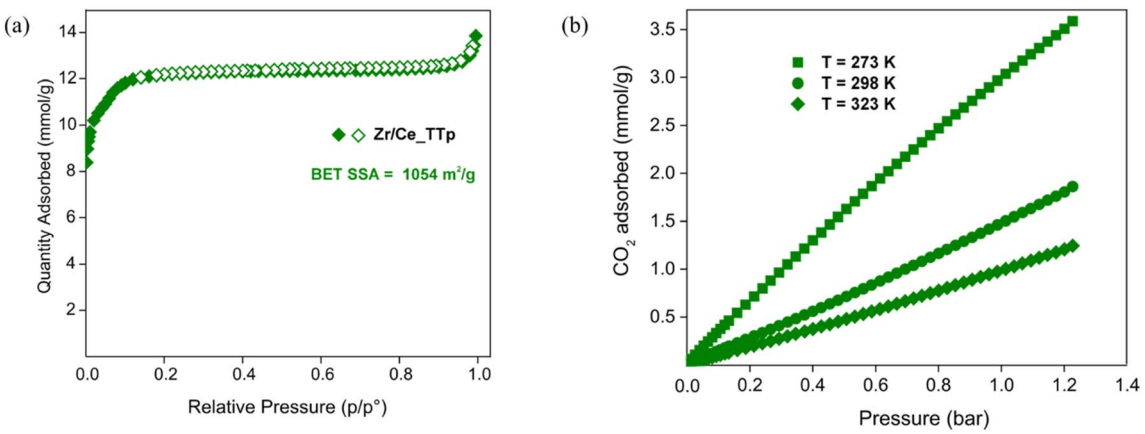

Fig. 5 (a) N_2 adsorption isotherm collected at $T = 77$ K on **Zr/Ce_TTp**. Empty symbols denote the desorption branch. (b) CO_2 adsorption isotherms collected at $T = 273$, 298 and 323 K on **Zr/Ce_TTp**.

has been tested for CO_2 adsorption at $p_{max} = 1.2$ bar and at variable temperatures: $T = 273$, 298 and 323 K (Fig. 5b). The CO_2 uptake at $p_{CO_2} = 1$ bar and $T = 298$ K is 6.6 wt% (1.5 mmol g^{-1}), much higher than that found in the zinc analogue [Zn_2(TTp)$_2$(bpy)] (2.3 wt%).[60] The CO_2 isosteric heat of adsorption at zero coverage (Q_{st}) has been calculated from the isotherms collected at the three temperatures applying the Clausius–Clapeyron equation. The value of 23 kJ mol^{-1} found is lower than that of [Zn_2(TTp)$_2$(bpy)] (31 kJ mol^{-1}),[60] because of the absence of a basic group (present in bpy) that is well-known to have a beneficial effect on the (acidic) CO_2 thermodynamic affinity of MOFs.[74–76] However, the enrichment of the microporous surface with polarizable sulphur atoms present in TTp^{2-} improves CO_2 adsorption through formation of multiple C–O···S stabilizing contacts, as proven by DFT calculations performed on [Zn_2(TTp)$_2$(bpy)].[60] The same kind of C–O···S interactions are also present in the DFT optimized structure of [CO_2@**Zr/Ce_TTp**] (*vide infra*).

Optical properties

The optical properties of **Zr_TTp**, **Ce_TTp** and **Zr/Ce_TTp** were investigated by UV-vis diffuse reflectance spectroscopy (DRS) and photoluminescence (PL) spectroscopy to elucidate their light absorption capabilities and charge recombination dynamics. The UV-vis DRS spectra (Fig. S13a) reveal that all materials exhibit strong absorption in the UV and visible regions. **Zr_TTp** and **Zr/Ce_TTp** show comparable absorption onsets at $\lambda \sim 365$ nm, corresponding to a bandgap of approximately 3.4 eV, as determined from the Tauc plots (Fig. S13b and d). **Ce_TTp** displays an extended absorption tail reaching into the visible region, with a narrower bandgap of ~3.0 eV (Fig. S13c). This red shift can be attributed to ligand-to-metal charge transfer (LMCT) transitions from the sulfur-containing TTp^{2-} ligand to the Ce^{IV} centers. Such transitions are characteristic of Ce-based MOFs and contribute to their visible-light harvesting ability.[23] Photoluminescence (PL) measurements were conducted to evaluate the recombination behavior of photoinduced electron–hole pairs, using a slightly different excitation wavelength for **Ce_TTp** with respect to that used for **Zr_TTp** and **Zr/Ce_TTp**, due to their different absorption edges as revealed by the UV-vis DRS spectra (Fig. S13). As shown in Fig. S14a, **Zr/Ce_TTp** exhibits a PL intensity and pattern comparable to those of **Zr_TTp**, with only minor differences. This similarity suggests that the incorporation of a small amount of Ce^{IV} does not significantly affect the overall recombination dynamics of the material. This is further supported by the nearly identical band gap values observed for the two MOFs, indicating that the electronic structure remains largely unperturbed by cerium insertion. In contrast, **Ce_TTp** displays multiple emission peaks (Fig. S14b) at $\lambda = 432$, 468, 586, and 620 nm. The multiple emission peaks observed in the PL spectra may reflect the presence of complex excited state pathways, including possible contributions from cerium-related electronic states and/or ligand-to-metal charge transfer (LMCT) processes.[23,77,78] While informative for the understanding of the photophysical features of **Ce_TTp**, the strong recombination-related luminescence suggests a limited photocatalytic efficiency for this material, consistent with its negligible activity in CO_2 reduction. Taken together, the optical characterization supports the conclusion that the improved photocatalytic performance of **Zr/Ce_TTp** does not stem from dramatic changes in light absorption or recombination behavior, but rather from subtle electronic effects introduced by the presence of the Ce^{IV}/Ce^{III} couple.

Photoelectrochemical properties

The photoelectrochemical behaviour of the synthesized MOFs was systematically evaluated to assess their ability to generate and transport photogenerated charges. Transient photocurrent responses under chopped light irradiation (Fig. 6a) clearly show that **Zr/Ce_TTp** exhibits a significantly higher and more stable photocurrent density compared to both **Zr_TTp** and **Ce_TTp**. This enhancement in photocurrent is indicative of a more efficient separation and transport of charge carriers, directly linked to the synergistic interaction between the Zr^{IV} and $Ce^{IV/III}$ metal centers in the mixed-metal framework. In contrast, the single-metal MOFs generate only weak photoresponses, highlighting the importance of bimetallic cooperation in achieving efficient light-driven charge dynamics.

The electrochemical activity of MOFs was verified through LSVs in CO_2 sat. 0.5 M Na_2SO_4 aqueous solution between −0.6 and −1.2 V. The analyzed samples show an onset potential of around −1.1 V (Fig. S15) for CO_2 reduction. For this reason, the potential of −1.1 V has been chosen to perform EIS analysis. A Randles equivalent circuit (inset of Fig. 6b), with a CPE constant phase element (Q), was used for the fitting analysis, as shown in Fig. S16.[79,80] The Nyquist plots (Fig. 6b) reveal that **Zr/Ce_TTp** has the smallest semicircle among the three materials, indicating the lowest charge transfer resistance (R_{CT}) for the electroreduction process (Table S3). On the other hand, **Ce_TTp** exhibits the largest impedance response, pointing to sluggish charge transport and poor conductivity, while **Zr_TTp** shows intermediate activity. These results agree with the photoelectrochemical behaviour. Mott–Schottky (MS) analysis (Fig. 6c) was used to determine the flat-band potentials (V_{fb}) and estimate the position of the conduction band (CB). All three MOFs show positive slopes in their MS plots, confirming their n-type semiconducting behavior. The extrapolated V_{fb} values (*vs.* $Ag/AgCl_{sat}$) are approximately −1.0 V (**Zr_TTp**), −1.3 V (**Zr/Ce_TTp**), and −0.7 V (**Ce_TTp**). These values translate to −0.80 V, −1.10 V, and −0.50 V *vs.* NHE, respectively, after conversion (+0.197 V). Assuming that the conduction band lies ~0.1 V more negative than V_{fb} for n-type materials, the CB positions are estimated to be −0.90 V for **Zr_TTp**, −1.20 V for **Zr/Ce_TTp**, and −0.60 V for **Ce_TTp** (*vs.* NHE). The significantly more negative CB position of **Zr/Ce_TTp** implies a stronger thermodynamic driving force for CO_2 photoreduction, consistent with its observed catalytic activity. The energy position of the valence-band could then be calculated according to:

$$E_{VB} = E_{CB} + E_g \quad (2)$$

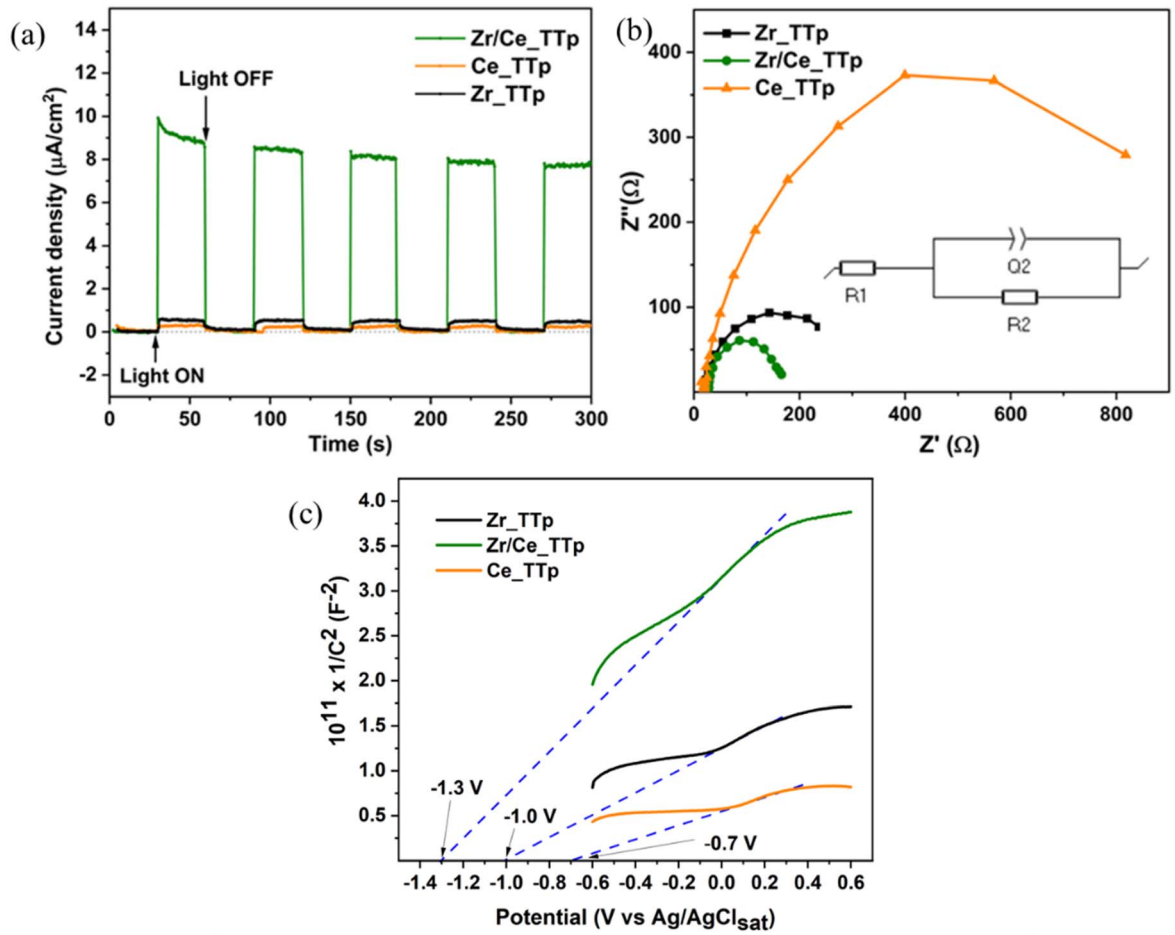

Fig. 6 (a) *I*–*t* curves, (b) EIS Nyquist plots and (c) Mott–Schottky plots of Zr_TTp, Ce_TTp and Zr/Ce_TTp.

where E_g is the band gap of the semiconductors. From these experimental magnitudes, the level diagram reported in Fig. S17 could be derived.

Photocatalytic CO_2 reduction performance

The photocatalytic CO_2 reduction activity of the three MOFs was evaluated under simulated solar irradiation using a 300 W xenon lamp. In a typical experiment, 5 mg of catalyst were dispersed in 5 mL of deionized water within a quartz Schlenk tube. After bubbling CO_2 for at least 30 minutes to ensure saturation, the system was sealed with a rubber septum and irradiated under continuous stirring. Gas-phase products were sampled after five hours of irradiation and analyzed using gas chromatography (GC). Among the tested materials, only bimetallic **Zr/Ce_TTp** exhibited detectable photocatalytic activity, producing carbon monoxide (CO) as the sole product with a total apparent quantum yield (AQY %) of 0.001% (see the SI). The formation rate was determined to be 5.8 μmol g^{-1} h^{-1}, indicating selective CO_2-to-CO conversion. No CH_4, H_2, or other gaseous products were observed under the employed conditions. Control experiments were performed to assess the origin of the detected product and to exclude possible artefacts. No CO formation was observed in the dark, confirming that the process is light-driven. Similarly, no gaseous product was detected in the blank experiment performed under UV-vis irradiation in a CO_2-saturated reaction medium and in the absence of a catalyst, ruling out direct photochemical CO formation from the reaction medium or reactor environment. The free H_2TTp linker did not produce CO under the same reaction conditions, excluding linker photodegradation as the origin of the detected product. Moreover, **Zr/Ce_TTp** did not generate CO under an inert He atmosphere, confirming that product formation requires the presence of CO_2. To further assess the role of the bimetallic framework, the corresponding monometallic analogues and their physical mixture (PM) were tested under CO_2 and no photocatalytic products was detected for **Ce_TTp** or **Zr_TTp** taken individually, while their PM afforded a CO production rate of 2.1 μmol g^{-1} h^{-1} (Fig. 7a). Although active, the physical mixture reached only *ca.* 36% of the activity of **Zr/Ce_TTp**, indicating that the improved photocatalytic performance cannot be explained by a simple additive contribution of the two homometallic phases. This comparison further supports the beneficial role of integrating Zr and Ce centers within the same framework. The catalytic results are consistent with literature reports on similar bimetallic Zr/Ce, Zr/Ti and Ce/Ti MOFs or MOF composites applied in photocatalytic CO_2

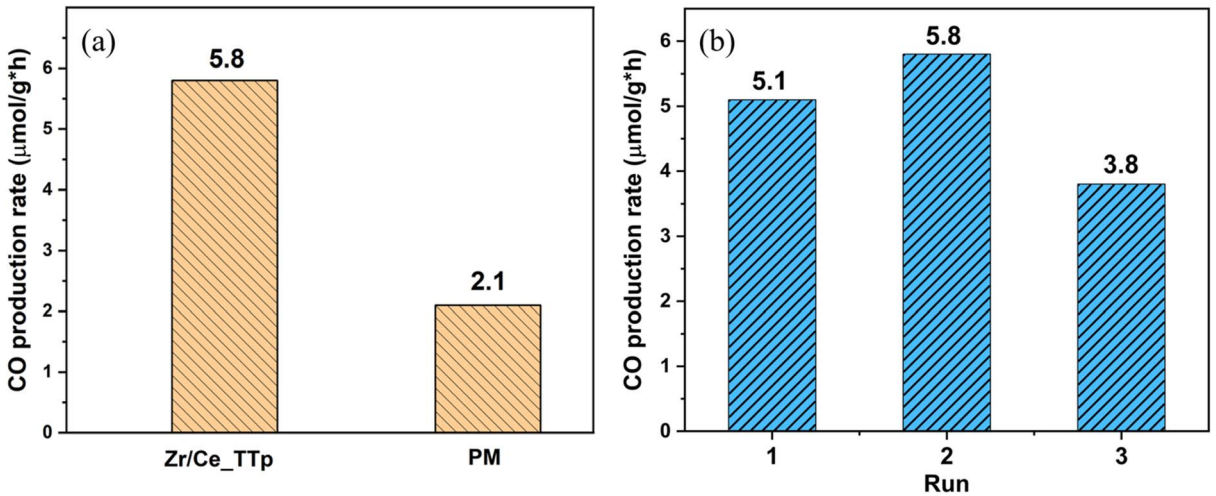

Fig. 7 (a) Comparison of the CO production rate of **Zr/Ce_TTp** and the physical mixture of **Zr_TTp** and **Ce_TTp**. (b) Recycling runs of **Zr/Ce_TTp**. CO gas was sampled after five hours of reaction for each cycle.

reduction (Table S4),[79,81,82] but to the best of our knowledge we present for the first time a bimetallic Zr/Ce MOF photocatalyst built with an heterocyclic organic linker. The incorporation of Ce into Zr-based frameworks has been shown to enhance charge separation, light absorption, and redox activity through the formation of Ce^{III}/Ce^{IV} redox pairs and improved ligand-to-metal charge transfer (LMCT) processes.[23,83,84] The observed photocatalytic behavior confirms that cerium incorporation not only modifies the electronic structure but also creates catalytically active sites capable of selectively reducing CO_2 to CO under mild aqueous conditions and without the need for sacrificial agents or co-catalysts. Furthermore, the S atoms present in the (thieno)thiophene linker improve the catalyst CO_2 absorption capacity,[60] strengthening the potential of TTp-based Zr/Ce-MOFs as efficient, noble-metal-free photocatalysts for sustainable CO_2 valorization. The stability of **Zr/Ce_TTp** was assessed through recycling tests; a 35% drop of CO production was recorded after three consecutive runs (for a total working time of 15 h), highlighting good stability under the chosen catalytic conditions (Fig. 7b). The structural and chemical stability of **Zr/Ce_TTp** after photocatalysis was further evaluated through PXRD, FT-IR and UV-vis spectroscopy (Fig. S18). The PXRD pattern recorded after the catalytic test retains the main reflections of the pristine material, particularly in the low-angle region, indicating that the framework is largely preserved under the reaction conditions. No additional reflections attributable to secondary crystalline phases are detected. In agreement with this, the FT-IR spectrum collected after photocatalysis maintains the characteristic vibrational features of the coordinated TTp^{2-} linker, without the appearance of new intense bands or the disappearance of the main framework-related signals. The UV-vis spectrum also preserves the overall absorption profile of the pristine material, although a slightly more extended absorption tail in the visible region is observed after catalysis. Overall, these results indicate that **Zr/Ce_TTp** retains its main structural, chemical and optical features after photocatalysis. With the aim of improving the photocatalytic performance of **Zr/Ce_TTp**, the catalytic trials were also conducted in the presence of different sacrificial agents or electron donor compounds such as triethanolamine (TEOA), triethylamine (TEA) and the sulfide/sulfite couple (Na_2S/Na_2SO_3); unfortunately, the MOF undergoes extensive decomposition in all cases before the start of the photocatalytic reaction.

DFT analysis of the electronic properties of Zr/Ce_TTp and its interaction with CO_2

A realistic model structure for the monometallic **Zr_TTp** and **Ce_TTp** MOFs has been obtained by removing two (thieno) thiophene-2,5-dicarboxylate groups from the Inorganic Building Unit (IBU) of the experimental CIF file and solving the S atom disorder on four equivalent positions in the TTp^{2-} linker generated by using the cubic crystal symmetry. Subsequently, the coordination vacancies were saturated with H_2O and OH^- groups to ensure the overall model electroneutrality. The bimetallic counterpart **Zr/Ce_TTp** is obtained by replacing one Zr atom in the IBU with Ce, resulting in two Ce atoms per unit cell. This choice was made to have the lowest possible cerium content in the model, given that in the real sample the number of cerium atoms is 0.04 per formula unit. First, the resulting structures were fully relaxed. Then, on top of the optimized structures, the highest occupied (HOCO) and lowest unoccupied (LUCO) crystalline orbitals were plotted, and the fundamental band gap was predicted.[23] Both monometallic **Zr_TTp** and **Ce_TTp** systems are characterized by the HOCO and LUCO that are delocalized on both the organic linker and the metal centers, with the HOCO dominated by the electronic levels of the TTp^{2-} linker, while the LUCO is mainly located on the metal node (Fig. S19–S22). The same composition is found in the bimetallic **Zr/Ce_TTp**, but, at odds with the homometallic materials, the frontier crystalline orbitals are more localized (Fig. 8). This different frontier orbital composition and shape may explain the difference in the photochemical activity shown

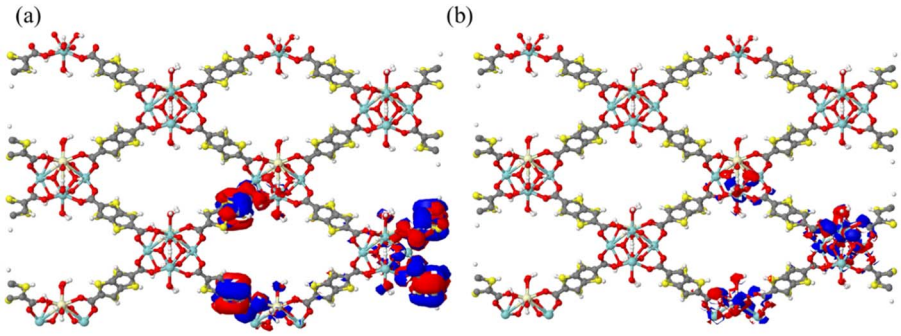

Fig. 8 (a) Highest occupied crystalline orbital (HOCO) and (b) lowest unoccupied crystalline orbital (LUCO) of **Zr/Ce_TTp**.

by **Zr/Ce_TTp** towards CO_2 reduction with respect to its homometallic counterparts. Indeed, photocatalytic activity in MOFs is strongly influenced by the nature and spatial distribution of their frontier orbitals. Although the concept is not to be considered of universal validity, it is commonly assumed that systems in which the HOCO and LUCO are spatially localized favor ligand-to-metal or metal-to-ligand charge transfer upon photoexcitation. This spatial separation promotes longer-lived charge-separated states and suppresses rapid electron–hole recombination, thereby enhancing interfacial redox reactivity. In contrast, MOFs featuring highly delocalized metal–ligand frontier orbitals often exhibit band-like electronic states that facilitate fast recombination, resulting in short excited-state lifetimes and limited photocatalytic efficiency.[85] The DFT predicted band gaps are in good agreement with the experimental data, especially for **Ce_TTp** and **Zr/Ce_TTp**, with computed values of 3.13 eV and 3.48 eV respectively, while **Zr_TTp** shows a slightly larger value of 4.15 eV. Finally, CO_2 adsorption was investigated on **Zr/Ce_TTp** with Ce^{III} ions as catalytically active sites. Since the XPS analysis (*vide supra*) reveals the presence of *ca.* 36% Ce^{III} in **Zr/Ce_TTp**, it is very likely that the cerium atoms in a lower oxidation state (generated by a partial electron transfer from TTp^{2-} after visible light irradiation) trigger CO_2 reduction, as observed in other literature studies.[79,81,82,86–88] The computational model was created by removing a OH^- group from Ce^{IV} and changing its atomic charge from +4 to +3, retaining the framework neutrality and creating a Ce^{III} exposed metal site. A closer inspection of the electrostatic potentials, reported in Fig. S23–S25, reveals positive (acidic) regions around the metal centres and negative (basic) regions on the carboxylic groups of the TTp^{2-} organic linkers. As expected, CO_2 interacts with the Ce^{III} Lewis acidic site through its oxygen atoms *via* non-covalent interactions as shown in Fig. 9 with an equilibrium $d(O{=}C{=}O\cdots Ce) = 2.863$ Å. It interacts with the surrounding oxygen atoms of the carboxylic groups [optimized $d(O_{TTp}\cdots C_{CO_2}) = 2.799$ Å] and interacts through its O atom with TTp^{2-} sulphur atoms [optimized $d(S\cdots O_{CO_2}) = 3.440$ Å]. Intriguingly, the S atoms on the linker bear a weakly positive charge that witnesses the ligand-to-metal electron transfer and concomitant $Ce^{IV} \rightarrow Ce^{III}$ reduction. The optimized $Ce^{III}\cdots O{=}C{=}O$ angle is 121.4°. The computed adsorption energy for the CO_2 interaction evaluated as $E(CO_2@MOF) - [E(CO_2) + E(MOF)]$ is -33.72 kJ mol^{-1}. To make a more reliable comparison with experimental results, we included the zero-point energy (E_{ZPE}) and the thermal correction to the enthalpy (H_T) at $T = 298$ K, which account for 5.88 kJ mol^{-1}. This gives a final interaction energy of -27.84 kJ mol^{-1}, which is in good agreement with the experimental Q_{st} value of 23 kJ mol^{-1}.

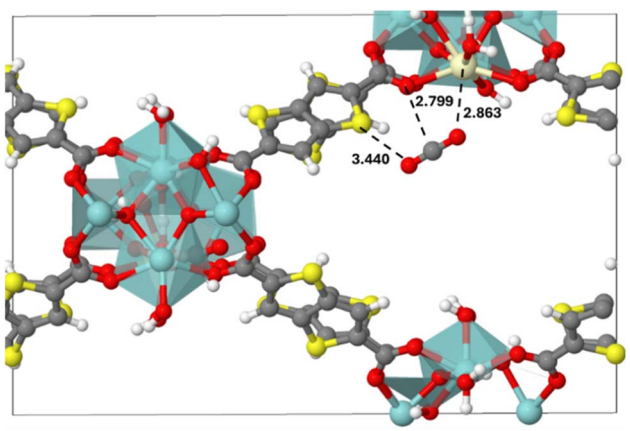

Fig. 9 Optimized unit cell of [CO_2@**Zr/Ce_TTp**]. Main gas-framework distances reported (Å). Atom colour code: H, white; C, grey; O, red; S, yellow; Zr, turquoise; Ce, sand.

Conclusions

This work reports the synthesis and comprehensive characterization of a novel bimetallic Zr/Ce-based MOF incorporating a π-conjugated (thieno)thiophene dicarboxylate linker and demonstrates its effectiveness as a photocatalyst for CO_2 reduction under simulated solar irradiation and in the absence of co-catalysts. The integration of structurally robust [Zr_6] oxo-clusters with redox-active cerium centres and a photoactive heterocyclic linker results in a well-defined, microporous framework exhibiting high surface area, favourable CO_2 adsorption affinity and enhanced photoelectrochemical properties. Compared to the corresponding monometallic analogues, the bimetallic system shows significantly improved photocatalytic activity and selective CO formation, highlighting the critical role of synergistic electronic interactions between Zr

and Ce centres. Experimental spectroscopic and electrochemical analyses supported by periodic DFT calculations reveal that cerium incorporation promotes improved charge separation, more favorable conduction band energetics and the formation of Ce^{III} catalytically active sites capable of stabilizing and activating CO_2 molecules. The combined structural stability, efficient charge carrier dynamics and noble-metal-free composition represent key strengths of this material and underscore the potential of heterometallic MOFs incorporating conjugated heterocyclic linkers as promising platforms for solar-driven carbon dioxide conversion. Future development in our laboratories aims at further optimizing the photocatalytic performance through precise control of metal composition, defect density, and the metal node electronic structure, as well as through the rational design of linkers with extended conjugation and enhanced visible-light absorption.

Author contributions

G. P.: conceptualization, investigation, formal analysis, writing – original draft; B. M., M. V. P., L. P., A. M., and B. D. B.: investigation, formal analysis; B. C. and G. G.: validation; L. D.: investigation, formal analysis, methodology, software, writing – original draft; S. G.: investigation, formal analysis, writing – original draft; A. R.: conceptualization, funding acquisition, project administration, supervision, writing – original draft.

Conflicts of interest

There are no conflicts to declare.

Data availability

CCDC 2536450 (**Zr_TTp**) and 2536451 (**Zr/Ce_TTp**) contain the supplementary crystallographic data for this paper.[89a,b]

The data supporting this article have been included as part of the supplementary information (SI). Supplementary information: additional characterization data (IR, UV-vis, photoluminescence spectra, XRF, PXRD, STEM-EDX, TG-MS, XPS, additional EXAFS data, pore size distribution, electrochemical plots, energy band plots) of **Zr/Ce_TTp**, Rietveld refinement plots of **Zr_TTp** and **Zr/Ce_TTp**, HOCO–LUCO plots of **Zr_TTp** and **Ce_TTp**, EPMs of all MOFs, and a collective table showing a comparison of the photocatalysis performance of **Zr/Ce_TTp** and other literature MOFs exploited in photocatalytic CO_2 reduction. See DOI: https://doi.org/10.1039/d6ta03759c.

Acknowledgements

G. P. and A. R. would like to acknowledge the European Union – NextGeneration EU from the Italian Ministry of Environment and Energy Security POR H2 AdP MMES/ENEA with involvement of CNR and RSE, PNRR – Mission 2, Component 2, Investment 3.5 "Ricerca e sviluppo sull'idrogeno", CUP: B93C22000630006 for funding. S. G. and A. M. acknowledge Università degli Studi dell'Insubria for partial funding. L. D. and B. C. gratefully acknowledge the support from the Project CH4.0 under the MUR program "Dipartimenti di Eccellenza 2023–2027" (CUP: D13C22003520001). M. V. P. acknowledges the Made in Italy – Circular and Sustainable (MICS) Extended Partnership funded by the European Union Next-Generation EU (Piano Nazionale di Ripresa e Resilienza (PNRR) – Missione 4, Componente 2, Investimento 1.3 – D. D. 1551.11-10-2022, PE00000004). L. P. gratefully acknowledges the technical support and access to the facilities provided by the Interdepartmental Research Unit "MatchLab" of the University of Florence and Mr Brunetto Cortigiani for his valuable technical assistance in the use of the platform. The European Synchrotron Radiation Facility (ESRF) is acknowledged for provision of synchrotron beamtime under proposal number EV-648. Drs Wouter van Beek, Dragos Costantin Stoian and Kenneth Marshall are also acknowledged for assistance and support in using beamline BM31. The BM31 setup was funded by the Swiss National Science Foundation (grant 206021_189629) and the Research Council of Norway (grant 296087). Dr Rocco Caliandro, Dr Cinzia Giannini and Dr Anna Moliterni (IC-CNR) are gratefully acknowledged for fruitful crystallographic discussions.

References

1 https://www.epa.gov/ghgemissions/overview-greenhouse-gases, https://climate.nasa.gov/vital-signs/carbon-dioxide/, https://unfccc.int/cop30.
2 R. Bala, M. Kaur, H. Thakur, P. Kashyap, A. Karnwal and T. Malik, *Int. J. Chem. Eng.*, 2025, **2025**, 7195300.
3 M. Rafique, D. Hussain, B. A. Kalwar, I. Ahmed, M. Hassan, L. Li, B. Wang, A. Mustafa, B. G. Lougou and Y. Shuai, *Inorg. Chem. Commun.*, 2025, **180**, 115136.
4 C. F. A. Rodrigues, H. Rocha, C. Tasinari and M. J. L. de Sousa, in *Carbon Capture Utilization and Storage: Law, Policy and Standardization Perspectives*, ed. E. G. Pereira, A. J. Fossa and T. L. Muinzer, Springer Nature Switzerland, Cham, 2025, pp. 35–85.
5 G. Singh, J. Lee, A. Karakoti, R. Bahadur, J. Yi, D. Zhao, K. AlBahily and A. Vinu, *Chem. Soc. Rev.*, 2020, **49**, 4360–4404.
6 Y. Chen, D. Wang, X. Deng and Z. Li, *Catal. Sci. Technol.*, 2017, **7**, 4893–4904.
7 C. Zhang, Y. Wu, D. Li and H.-L. Jiang, *Chem. Sci.*, 2025, **16**, 13149–13172.
8 P. Verma, R. V. Singh, A. M. Banerjee and M. R. Pai, *Int. J. Hydrogen Energy*, 2025, **107**, 569–585.
9 M. Shanmugam, P. J. J. Sagayaraj, P. Mani, L. P. Sl, N. K. Thimmarayampalayam Ramasamy, M. S. Yesupatham, H.-i. Kim, B. Neppolian and K. Sekar, *ACS Appl. Eng. Mater.*, 2025, **3**, 1927–1942.
10 S. Mumtaz, M. A. Nazir, S. S. A. Shah, H. K. Thabet, Z. M. El-Bahy, S. Bibi, M. A. Wattoo and A. u. Rehman, *Adv. Sustain. Syst.*, 2025, **9**, 2400852.
11 H. Ali, O. Iqbal, B. Al Alwan, A. Abdulrahman, Y. Orooji, E. S. Al-Farraj, M. Sadiq, S. Imran, A. M. Abu-Dief, D. Yue and A. Hayat, *Coord. Chem. Rev.*, 2025, **541**, 216822.

12 H. García and S. Navalón, *Metal-Organic Frameworks: Applications in Separations and Catalysis*, ed. H. García and S. Navalón, Wiley-VCH Verlag GmbH & Co. KGaA, 2018.
13 S. Kaskel, *The Chemistry of Metal–Organic Frameworks: Synthesis, Characterization, and Applications*, ed. S. Kaskel, Wiley-VCH Verlag GmbH & Co. KGaA, 2016, vol. 1.
14 D. Farrusseng, *Metal-Organic Frameworks: Applications from Catalysis to Gas Storage*, ed. D. Farrusseng, Wiley-VCH Verlag GmbH & Co. KGaA, 2011.
15 https://www.nobelprize.org/prizes/chemistry/2025/summary/.
16 J. Zhou, S. Gu, Y. Xiang, Y. Xiong and G. Liu, *Coord. Chem. Rev.*, 2025, **526**, 216354.
17 X. Yan and W. Lin, *Coord. Chem. Rev.*, 2025, **545**, 217034.
18 Y. Xue and J. W. Chew, *J. Mater. Chem. A*, 2025, **13**, 11989–12008.
19 D. Cartagenova, F. A. Peixoto Esteves, N. T. Fischer, J. A. van Bokhoven and M. Ranocchiari, *Inorg. Chem. Front.*, 2022, **9**, 70–77.
20 H. Molavi, *Coord. Chem. Rev.*, 2025, **527**, 216405.
21 Q.-J. Wu, J. Liang, Y.-B. Huang and R. Cao, *Acc. Chem. Res.*, 2022, **55**, 2978–2997.
22 J. Jacobsen, A. Ienco, R. D'Amato, F. Costantino and N. Stock, *Dalton Trans.*, 2020, **49**, 16551–16586.
23 X.-P. Wu, L. Gagliardi and D. G. Truhlar, *J. Am. Chem. Soc.*, 2018, **140**, 7904–7912.
24 A. Chandran P, G. Radha, P. C. Meenu, S. Roy and H. Aggarwal, *Mater. Adv.*, 2024, **5**, 6936–6943.
25 S. Ren, J. Dong, X. Duan, T. Cao, H. Yu, Y. Lu and D. Zhou, *Chem. Eng. J.*, 2023, **460**, 141884.
26 M. Ronda-Lloret, I. Pellicer-Carreño, A. Grau-Atienza, R. Boada, S. Diaz-Moreno, J. Narciso-Romero, J. C. Serrano-Ruiz, A. Sepúlveda-Escribano and E. V. Ramos-Fernandez, *Adv. Funct. Mater.*, 2021, **31**, 2102582.
27 G. Mercuri, G. Giambastiani and A. Rossin, *Inorganics*, 2019, **7**, 144.
28 S. S. M. Fernandes, M. C. R. Castro, A. I. Pereira, A. Mendes, C. Serpa, J. Pina, L. L. G. Justino, H. D. Burrows and M. M. M. Raposo, *ACS Omega*, 2017, **2**, 9268–9279.
29 C. Zhang and X. Zhu, *Acc. Chem. Res.*, 2017, **50**, 1342–1350.
30 A. Zhang, H. Xiao, S. Cong, M. Zhang, H. Zhang, S. Bo, Q. Wang, Z. Zhen and X. Liu, *J. Mater. Chem. C*, 2015, **3**, 370–381.
31 S. L. Estes, M. R. Antonio and L. Soderholm, *J. Phys. Chem. C*, 2016, **120**, 5810–5818.
32 A. M. Samsonova, V. A. Bolotov, D. G. Samsonenko, D. N. Dybtsev and V. P. Fedin, *J. Struct. Chem.*, 2019, **60**, 1468–1473.
33 N. Fairley, V. Fernandez, M. Richard-Plouet, C. Guillot-Deudon, J. Walton, E. Smith, D. Flahaut, M. Greiner, M. Biesinger, S. Tougaard, D. Morgan and J. Baltrusaitis, *Appl. Surf. Sci. Adv.*, 2021, **5**, 100112.
34 A. J. Barlow, S. Popescu, K. Artyushkova, O. Scott, N. Sano, J. Hedley and P. J. Cumpson, *Carbon*, 2016, **107**, 190–197.
35 R. Caliandro, C. Favia and R. Lassandro, *Structure-Based Optimization of Metal-Organic Frameworks (MOFs) for Green Energy Applications [ZrCe_TTp]*, European Synchrotron Radiation Facility, 2028.
36 B. Ravel and M. Newville, *J. Synchrotron Radiat.*, 2005, **12**, 537–541.
37 S. Smolders, A. Struyf, H. Reinsch, B. Bueken, T. Rhauderwiek, L. Mintrop, P. Kurz, N. Stock and D. E. De Vos, *Chem. Commun.*, 2018, **54**, 876–879.
38 Topas, *V. 3.0; Bruker AXS*, Karlsruhe, Germany, 2005.
39 A. Le Bail, H. Duroy and J. L. Fourquet, *Mater. Res. Bull.*, 1988, **23**, 447–452.
40 J. H. Cavka, S. Jakobsen, U. Olsbye, N. Guillou, C. Lamberti, S. Bordiga and K. P. Lillerud, *J. Am. Chem. Soc.*, 2008, **130**, 13850–13851.
41 R. W. Cheary and A. A. Coelho, *J. Appl. Crystallogr.*, 1992, **25**, 109–121.
42 Geometrical parameters of the rigid body describing the TTp^{2-} linker. Bond distances (Å): C–C 1.40, C–S 1.70, C–O 1.25 Å, C–H 0.95; bond angles (°): endocyclic C–C–C 112, exocyclic C–C–S and, *C–C–O***120**124.
43 Geometrical parameters of the rigid body describing the DMF molecule. Bond distances (Å): C–N 1.45, C═O 1.25, C–H 0.95; bond angles (°): O–C–N and H–C–N 120, C–N–C and H–C–H 109.5.
44 A. Coelho, *J. Appl. Crystallogr.*, 2000, **33**, 899–908.
45 H. M. Rietveld, *J. Appl. Crystallogr.*, 1969, **2**, 65–71.
46 D. A. Gómez-Gualdrón, P. Z. Moghadam, J. T. Hupp, O. K. Farha and R. Q. Snurr, *J. Am. Chem. Soc.*, 2016, **138**, 215–224.
47 X. Zhu, C. Tian, G. M. Veith, C. W. Abney, J. Dehaudt and S. Dai, *J. Am. Chem. Soc.*, 2016, **138**, 11497–11500.
48 X. Zhu, S. M. Mahurin, S.-H. An, C.-L. Do-Thanh, C. Tian, Y. Li, L. W. Gill, E. W. Hagaman, Z. Bian, J.-H. Zhou, J. Hu, H. Liu and S. Dai, *Chem. Commun.*, 2014, **50**, 7933–7936.
49 L. Doná, J. G. Brandenburg and B. Civalleri, *J. Chem. Phys.*, 2019, **151**, 121101.
50 A. Erba, J. K. Desmarais, S. Casassa, B. Civalleri, L. Donà, I. J. Bush, B. Searle, L. Maschio, L. Edith-Daga, A. Cossard, C. Ribaldone, E. Ascrizzi, N. L. Marana, J.-P. Flament and B. Kirtman, *J. Chem. Theory Comput.*, 2023, **19**, 6891–6932.
51 L. Donà, J. G. Brandenburg and B. Civalleri, *J. Chem. Phys.*, 2022, **156**, 094706.
52 J. P. Perdew, A. Ruzsinszky, G. I. Csonka, O. A. Vydrov, G. E. Scuseria, L. A. Constantin, X. Zhou and K. Burke, *Phys. Rev. Lett.*, 2008, **100**, 136406.
53 S. Grimme, S. Ehrlich and L. Goerigk, *J. Comput. Chem.*, 2011, **32**, 1456–1465.
54 H. Kruse and S. Grimme, *J. Chem. Phys.*, 2012, **136**, 154101.
55 R. M. Hanson and X.-J. Lu, *Nucleic Acids Res.*, 2017, **45**, W528–W533.
56 P. A. Demakov, V. A. Lazarenko, P. V. Dorovatovskii and V. P. Fedin, *J. Struct. Chem.*, 2023, **64**, 2417–2426.
57 P. A. Demakov, D. N. Dybtsev and V. P. Fedin, *Chem. Commun.*, 2023, **59**, 9380–9383.
58 Y. A. Yudina, P. A. Demakov, A. A. Ryadun, V. P. Fedin and D. N. Dybtsev, *Crystals*, 2022, **12**, 1374.
59 P. A. Demakov, A. A. Ryadun and D. N. Dybtsev, *Molecules*, 2022, **27**, 8055.

60 V. A. Dubskikh, K. A. Kovalenko, A. S. Nizovtsev, A. A. Lysova, D. G. Samsonenko, D. N. Dybtsev and V. P. Fedin, *Nanomaterials*, 2022, **12**, 4281.
61 K. Koh, A. G. Wong-Foy and A. J. Matzger, *J. Am. Chem. Soc.*, 2009, **131**, 4184–4185.
62 J. L. C. Rowsell and O. M. Yaghi, *J. Am. Chem. Soc.*, 2006, **128**, 1304–1315.
63 A. Ghorbani, S. A. Mousavi and H. Molavi, *Langmuir*, 2025, **41**, 19776–19788.
64 S. Yoon, J. Jo, B. Jeon, J. Lee, M. G. Cho, M. H. Oh, B. Jeong, T. J. Shin, H. Y. Jeong, J. Y. Park, T. Hyeon and K. An, *ACS Catal.*, 2021, **11**, 1516–1527.
65 J. A. Rodriguez, S. Ma, P. Liu, J. Hrbek, J. Evans and M. Pérez, *Science*, 2007, **318**, 1757–1760.
66 C. Qiu, A. Kumar, D. Qiu, M. Tabish, J. Zhang, Z. Jiang, A. Li, G. Yasin, X. Chen and H. Song, *J. Mater. Chem. A*, 2023, **11**, 22187–22197.
67 F. Li, L. Sun, Y. Luo, M. Li, Y. Xu, G. Hu, X. Li and L. Wang, *RSC Adv.*, 2018, **8**, 19635–19641.
68 Y. Su, Y. Zhang, X. Zhuang, S. Li, D. Wu, F. Zhang and X. Feng, *Carbon*, 2013, **62**, 296–301.
69 C. D. Wagner, A. V. Naumkin, A. Kraut-Vass, J. W. Allison, C. J. Powell and J. R. J. Rumble. *NIST Standard Reference Database 20, Version 3.4 (web version)*.
70 D. Barreca, G. A. Battiston, R. Gerbasi, E. Tondello and P. Zanella, *Surf. Sci. Spectra*, 2000, **7**, 303–309.
71 The diameter of the cavities was estimated as the diameter of a sphere inscribed in a tetrahedron or an octahedron whose edge was the shortest Zr⋯Zr distance between two nodes.
72 The empty volume, amounting to 55% for **Zr_TTp** and 54% for **Zr/Ce_TTp**, was estimated using the software Mercury 2024.3.1, employing a probe with radius 1.2 Å and a grid spacing of 0.3 Å.
73 X. Na, S. Xing, M. Tan and W. Su, *Adv. Sci.*, 2024, **11**, 2409451.
74 P. Campitelli, A. Tombesi, C. Di Nicola, C. Pettinari, A. Mauri, S. Galli, T. Yan, D. Liu, J. D. Duan, S. Goswami, G. Tuci, G. Giambastiani, J. T. Hupp and A. Rossin, *ACS Appl. Energy Mater.*, 2023, **6**, 9231–9242.
75 G. Mercuri, M. Moroni, K. V. Domasevitch, C. Di Nicola, P. Campitelli, C. Pettinari, G. Giambastiani, S. Galli and A. Rossin, *Chem.–Eur. J.*, 2021, **27**, 4746–4754.
76 P. Müller, B. Bucior, G. Tuci, L. Luconi, J. Getzschmann, S. Kaskel, R. Q. Snurr, G. Giambastiani and A. Rossin, *Mol. Syst. Des. Eng.*, 2019, **4**, 1000–1013.
77 E. E. Ghadim, M. Walker and R. I. Walton, *Dalton Trans.*, 2023, **52**, 11143–11157.
78 J. G. Knapp, D. Ray, P. B. Calio, M. C. Wasson, T. R. Scott, L. Gagliardi and O. K. Farha, *Chem. Commun.*, 2022, **58**, 525–528.
79 W. Wang, S. Song, P. Wang, M. He, Z. Fang, X. Yuan, H. Li, C. Li, X. Wang, Y. Wei, W. Song, H. Xu and Z. Li, *ACS Catal.*, 2023, **13**, 4597–4610.
80 J. E. B. Randles, *Discuss. Faraday Soc.*, 1947, **1**, 11–19.
81 C. Yu, X. Zhang, C. Song, Y. Wang, J. Lin, Z. Guo, Y. Zhang, Z. Liu, C. Li, Y. Sun, C. Tang and Y. Huang, *Chem. Eng. J.*, 2024, **499**, 156088.
82 S. Li, H. Li, Y. Wang, Q. Liang, M. Zhou, D. Guo and Z. Li, *Sep. Purif. Technol.*, 2024, **333**, 125994.
83 V. Finelli, S. Rojas-Buzo, M. Signorile, F. Bonino and S. Bordiga, *Nano Mater. Sci.*, 2025, **7**, 761–772.
84 A. Bhattacharyya, M. Gutiérrez, B. Cohen, H. Szalad, J. Albero, H. Garcia and A. Douhal, *ACS Appl. Mater. Interfaces*, 2023, **15**, 36434–36446.
85 C.-Y. Wang, H.-E. Chang, C.-Y. Wang, T. Kurioka, C.-Y. Chen, T.-F. Mark Chang, M. Sone and Y.-J. Hsu, *Nanoscale Adv.*, 2024, **6**, 1039–1058.
86 M. Shen, L. Wang, M. Zhou, L. Lin, H. Li, Y. Wang, S. Xu and Z. Li, *Fuel*, 2025, **396**, 135403.
87 S. Payra, S. Ray, R. Sharma, K. Tarafder, P. Mohanty and S. Roy, *Inorg. Chem.*, 2022, **61**, 2476–2489.
88 D. Sun, W. Liu, M. Qiu, Y. Zhang and Z. Li, *Chem. Commun.*, 2015, **51**, 10765.
89 (*a*) CCDC 2536450: Experimental Crystal Structure Determination, 2026, DOI: 10.5517/ccdc.csd.cc2r4cz8; (*b*) CCDC 2536451: Experimental Crystal Structure Determination, 2026, DOI: 10.5517/ccdc.csd.cc2r4d0b.